MAGNETIC THIN FILM SHIELDINGS ON ELECTRICAL WIRES

BY

CHAONAN CHEN

A THESIS
SUBMITTED TO THE FACULTY OF

ALFRED UNIVERSITY

IN PARTIAL FULFILLMENT OF THE REQUIREMENTS
FOR THE DEGREE OF

MASTER OF SCIENCE

IN

ELECTRICAL ENGINEERING

ALFRED, NEW YORK

MAY, 2003

MAGNETIC THIN FILM SHIELDINGS ON ELECTRICAL WIRES

BY

CHAONAN CHEN

SIGNATURE OF AUTHOR_____(Signature on file)_____

APPROVED BY_____(Signature on file)_____
XINGWU WANG, ADVISOR

_____(Signature on file)_____
JOSEPH ROSICZKOWSKI, ADVISORY COMMITTEE

_____(Signature on file)_____
WALLACE B. LEIGH, ADVISORY COMMITTEE

_____(Signature on file)_____
JAMES LANCASTER, CHAIR, ELECTRICAL ENGINEERING

ACCEPTED BY_____(Signature on file)_____
DAVID SZCZERBACKI, ACTING DEAN
OF ENGINEERING

Acknowledgements

The author would like to thank Dr. Xingwu Wang for his guidance, patience, and encouragement during the study.

Many thanks also to Mr. Ron Miller for his work of thin film coatings, Mr. Ward Votava for his help with SEM/EDS and AFM experiments, Mr. Slawomir I. Idzieszynsli for his help with XRD analysis, Mr. Brett Schulz for his help with laser interference analysis, Mr. Yuandan Liu for his calculation on XRD results, Dr. Peter Lubitz of NRL, SUNY Buffalo for magnetize measure, Dr. Jack Lin of Intersil Co. for some of SEM/EDS results, Dr. Wallace B. Leigh for his literature help, Dr. Joseph Rosiczkowski for his support, Ms. Rosalie DiRaimondo for her constant support.

Ms. Carla Coch and Ms. Pat LaCourse helped me finish the text revision.

Gratitude is extended to Mr. Cody Washburn for his help in the lab, Mr. Huihui Duan and Ms. Mingming Duan for their daily support and encouragement.

I also wish to thank Dr. James T. Lancaster for his support.

This work is partially supported by the Biophan Technology Inc. and Intersil Co.

All modeling results were obtained with modeling tools called “Maxwell 2D”, Maxwell 2D are owned by and registered trademarks of Ansoft Corporation, Pittsburgh, PA.

Table of Contents

Page

List of Tables

List of Figures

Abstract

Magnetic Resonance Imaging (MRI) is a well-established diagnostic technique in clinical medicine. However, many patients with implanted medical devices cannot benefit from such an important diagnostic tool; the major reason for this is electromagnetic interference. The principle bio-effect is heating in the electrical wires of the implanted medical devices. One way to solve this problem is to shield the electrical wires from the magnetic field of MRI. This study focuses on determining the shielding effects of a thin film coated aluminum rod that simulates an electrical wire of implanted medical devices, such as cardiac pacemakers and spinal cord stimulators.

A multi-layer thin film is coated onto the surface of the electrical wire. Experimentally, several different kinds of thin films, including aluminum nitride and aluminum iron, are deposited either on the silicon wafer or the aluminum rod by a sputtering deposition technique. Then several critical shielding properties of the as-deposited films are characterized using different methods.

The heating effects are related to power loss induced by the RF magnetic field of MRI. Magnetic flux density and power loss are used as the parameters for shielding effect comparison. Computer simulations are performed to examine how the magnetic flux density and power loss are affected by the shell thickness, conductivity, and permeability.

Temperature increases in the wire without shielding and with shielding is calculated from the simulation results of power loss. Therefore, optimal thin film shielding parameters are suggested to keep the heating effects in the wire at acceptable levels.

1. Introduction

1.1 Background of magnetic resonance imaging (MRI)

1.1.1 Concept for MRI

Many new imaging techniques have been developed in the past decades, such as computed tomography (CT), ultrasonic imaging, and magnetic resonance imaging (MRI).

MRI is a noninvasive technique that uses no ionizing radiation or contrast medium to produce high quality images of the internal parts of the human body.[1]

1.1.2 Principle of MRI

MRI is based upon the radio frequency (RF) signal, which is emitted by hydrogen nuclei of tissues after they have been perturbed by RF pulses in the presence of strong magnetic field. [1]

In a magnetic resonance imager, there are three sets of magnetic coils: magnet coil, gradient coil, and radio frequency coil. Figure 1 displays a schematic representation of the three sets of coils.

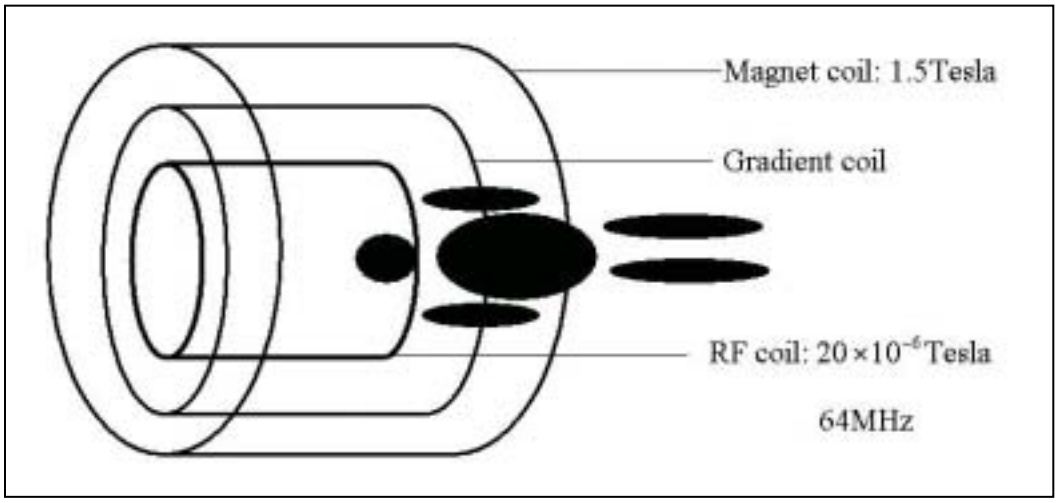

Figure 1. MRI system diagram

The human body is composed of a very large number of protons (water and fat molecules mostly), which are spinning due to their inherent charge. These spins are

generally incoherent, causing a net zero spin. The magnet coil produces the DC B_0 field for the imaging procedure. The typical value of B_0 is 1.5 tesla.[2] It is responsible for aligning hydrogen protons in the human body.

The gradient coils produce a gradient in B_0 field. The gradient coils are pulsed on and off during and between RF excitation pulses to spatially encode information contained in the emitted RF signal.

The RF coil creates the B_1 field that rotates the net magnetization in a pulse sequence. The typical frequency is 64MHz.[2] In the presence of the RF magnetic field, the nuclei of hydrogen atoms can be made to behave as tiny radio transmitters and emit radio waves as a signal. The RF coil also works as receiver to pick up the RF energy from the imaged object.

1.1.3 Application of MRI

MRI has evolved rapidly into an accepted modality for medical imaging of diagnosis processes. Now, it has been frequently used for diagnosis of virtually every major pathological condition. Examples are in brain abscess, cardiovascular disease, liver disease, renal disease, neurocysticerosis, psychiatric disorders, and tumor size evaluation.

1.1.4 Effect of MRI on implanted medical devices

In the current clinic medicine treatment field, except for traditional drug therapy and surgical measures, implanted devices played increasingly important roles. For example, elastic graduated compression stockings can be used to support the veins; this is the best non-operative approach for the management of varicose veins[1]. A septal occlusion device can be implanted in the heart through the femoral vein to cure atrial septal defect (ASD). A cardiac pacemaker can be implanted for either atrial or ventricular pacing. Spinal cord stimulators are designed to provide relief from chronic pain.

To implant devices such as these or monitor their position in the human body, a technique to produce detail imaging for both the device and the surrounding tissue is necessary. Although MRI is a well-established imaging technique to produce detailed imaging for the internal parts of human body, most of the implanted devices are not

compatible with MRI because of the electromagnetic interference between the strong magnetic field produced during MRI and certain implanted devices, especially cardiac pacemakers. Typically, a pacemaker has a pulse generator and one or two pacing leads. Pacing leads are usually inserted transvenously through the subclavian or cephalic vein with the leads positioned in the right atrial appendage for atrial pacing or the right ventricular apex for ventricular pacing. The leads are then attached to the pulse generator, which is inserted into a subcutaneous pocket below the clavicle. The pulse generator includes sophisticated electronic circuitry that monitors cardiac activity and initiates a current when necessary.[1] Fully contraindicated during MRI, the cardiac pacemaker is affected by the strong magnetic fields, magnetic field gradients, and radio frequency energy used in MRI.

Strong magnetic fields can induce currents in the pacemaker circuitry, which cause it to fail and possibly result in death for the patient wearing a pacemaker. It was reported that magnetic field strength as low as 10 gauss may be sufficient to cause deflection or programming changes or to close the reed switch and convert a pacemaker to an asynchronous mode. Even outside the scan room, fringing B fields can affect the operation of the cardiac pacemaker. The United States Food and Drug Administration (USFDA) safety guidelines state that people with pacemakers must not be exposed to magnetic fields greater than 5 gauss.[3]

When the wire carries current under the static magnetic field, it experiences a Lorentz force, which then produces a torque on the wire. These effects may result in damage to both the wire and local tissue. Even in the patient whose pacemaker has been removed, the remaining pacing lead can act as an antenna and induce currents, causing cardiac fibrillation.

Another problem occurs when the RF energy from an imaging sequence causes heating in the tissues of the body. Eddy current is induced when an electrical wire is exposed to the RF magnetic field which results in power loss that is converted to heat. Significant heating is due to the inability to dissipate heat. The USFDA recommends that exposure to RF energy be limited. Any pulse sequence must not raise the temperature by more than 1^{o} Celsius.[4]

MRI is a very useful diagnostic imaging technique. More and more people prefer to have an implanted device than have operation because of safety, reduced tissue damage, and faster recovery. Electromagnetic interference is the biggest problem between MRI and an implanted device that prevents them being used together. (See Figure 2.) Many scientists and engineers are trying to solve the problem of electromagnetic interference. Much more attention has been paid to the heating effects of the MRI on the implanted medical device rather than to reducing the heating effect itself. There is currently no MRI compatible pacemaker or stimulator in the market. In this paper, we will concentrate on the power loss produced by the RF magnetic field which subsequently causes heating of the electrical wires during MRI.

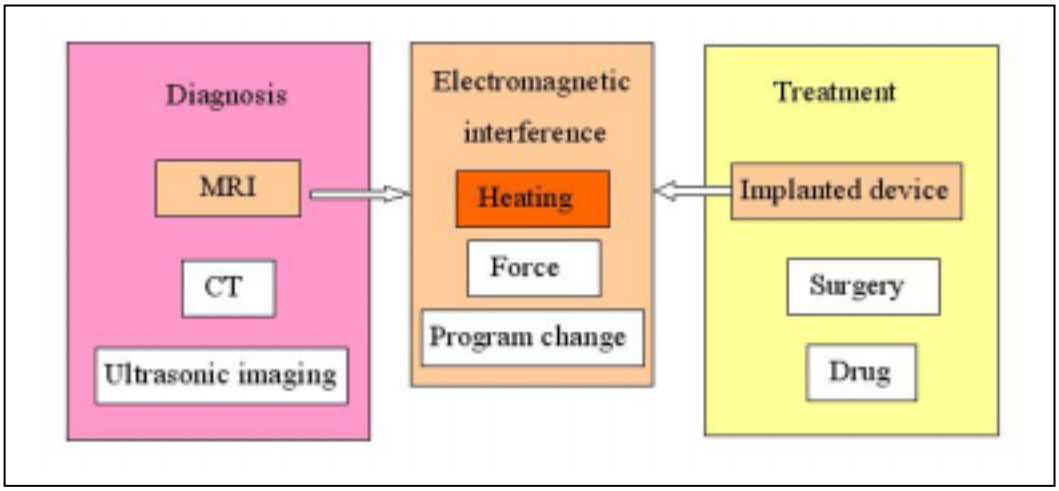

Figure 2. Electromagnetic interference of MRI on implanted device

A possible solution for this heating effect is to shield the electrical wires from the RF magnetic field. Computer simulations on the shielding effects have been performed and will be discussed in Chapter 3.

The work scope of this paper is explained below.

1.2 Scope of work

1.2.1 Solution model

Modern technology requires multiple properties from materials, but a single or monolithic material cannot meet such demands in high technology applications. A

composite material, such as a core material and a coating, each with the requisite properties to fulfill the specifications, is needed. The idea of such a composite material is examined in this research to solve the electromagnetic interference problem between the RF magnetic field in MRI and the electrical wire of an implanted medical device.

Figure 3 illustrates the thin film shielding model for an electrical wire. The inner rod represents an electrical wire. The outer, shielding layer is coated on the surface of the wire. An insulating layer is inserted between them to avoid an electrical current flow between the electrical wire and shielding layer.

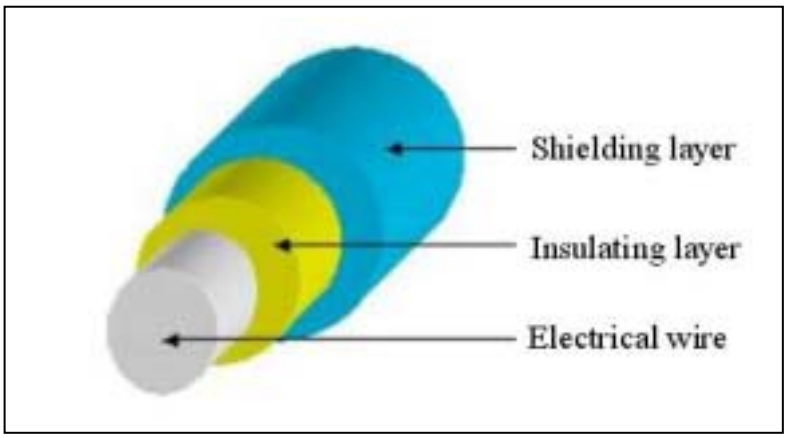

Figure 3. Electrical wire thin film coating model

1.2.2 Material investigation

Shielding is a possible solution for reducing the power loss related heating effects of the RF magnetic field on the electrical wire. Magnetic fields can penetrate non-magnetic materials; however, these fields have a tendency to be attracted by high-permeability magnetic materials. As the magnetic permeability becomes larger, this effect becomes stronger. Therefore a material with high permeability should be an ideal candidate as a magnetic shielding material.

Iron-containing magnetic materials such as AlFe have been fabricated by various techniques. Magnetic properties of these materials vary with stoichiometric ratios, particle size, and fabrications. When the iron molar ratio in bulk AlFe materials is less than 70%, the material exhibits very weak magnetism. In contrast to bulk materials, thin film materials exhibit different magnetic properties due to constraints provided by the substrate. In this paper, AlFe thin films are studied for magnetic shielding purposes.

The composite material coated on the wire should also have two more properties: low electrical conductivity and high thermal conductivity. Aluminium nitride (AlN) is well known for its low electrical conductivity and high thermal conductivity (second only to Beryllium). Due to its unique material properties, an AlN thin film is selected as the material for the insulating layer; it also provides a more efficient cooling effect than a conventional insulator.

To get first hand information about the materials described above, we coated AlN and AlFe films separately onto the surface of a silicon wafer using DC or pulsed DC magnetron sputtering techniques. The properties of these films were analyzed using different methods, such as SEM, EDS, SQUID, XRD, and AFM.

The film deposition and film characterization will be discussed in Chapter 2.

1.2.3 Computer simulation

After the properties of coated films were obtained, we assessed the electromagnetically induced effects using Maxwell 2D eddy current solver model in Ansoft Maxwell EM software package.[5] The thickness, permeability, and conductivity of the insulating material and shielding material are necessary inputs for computer simulations. Maxwell computer simulation models are explained in Chapter 3. Magnetic flux density and power loss are used as the parameters for shielding effect comparison. Computer simulations are performed to examine how the shielding effects are affected by shielding thickness, conductivity, and permeability.

1.2.4 Temperature calculation

Temperature increases in the wire without shielding and with shielding is calculated from the power loss. Optimal shielding parameters for better temperature control are suggested.

2. Thin Film Deposition and Characterization

There are two classes of thin film deposition methods: Chemical Vapor Deposition (CVD) and Physical Vapor Deposition (PVD). The latter usually includes techniques of evaporation, ion planting, and sputtering. In our experiments, a sputtering technique is utilized.

2.1 Thin film sputtering deposition

Sputtering is a process that occurs as a result of the momentum exchange collision cascade process initiated near the surface of the target (the source of the coating material) by an incidental energetic projectile. Typically, Argon (Ar) is used as the inert gas because of its mass compatibility with materials of engineering interest, low cost, and ease of being ionized.

2.1.1 Sputtering techniques

There are four techniques for sputtering deposition: DC sputtering, pulsed DC sputtering, RF sputtering, and magnetron sputtering.

2.1.1.1 DC sputtering

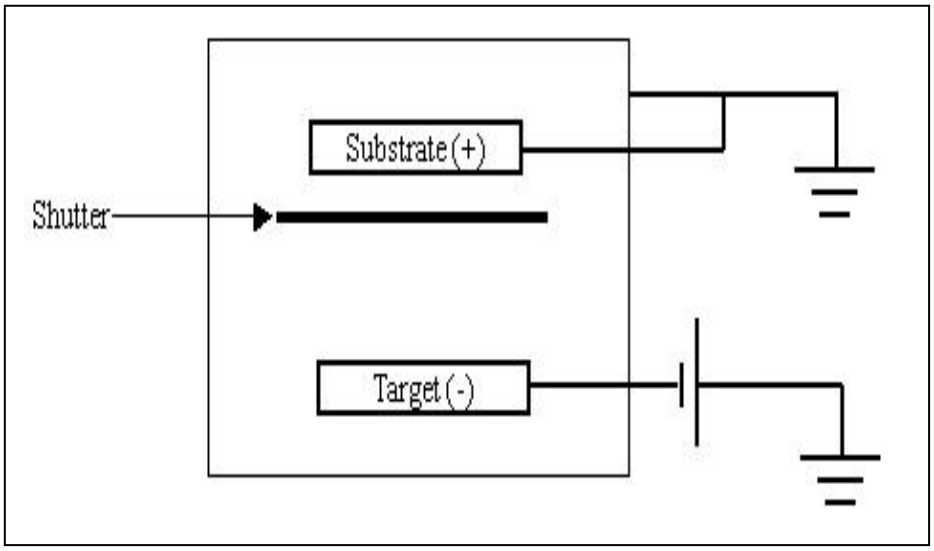

Figure 4. Schematic of DC sputtering

DC sputtering is powered by a DC power supply. As Figure 4 shows, it consists of two parallel electrodes: a cathode and an anode. Between the two electrodes, a shutter is used before sputtering. A negative potential is applied to the target (cathode). The substrate (anode) is grounded. A low-pressure glow discharge (about 10-3 torr) is maintained between the cathode and the anode. During operation, Ar atoms become ionised; then the ions are accelerated across the potential gradient of the cathode sheath and collide with the target causing sputtering of the surface.

Among the three sputtering deposition techniques, DC sputtering is the simplest and most widely used. However, DC sputtering cannot be used to sputter non-conducting targets because of charge accumulation at the target surface. There are two ways to produce dielectric films: pulsed DC sputtering and radio frequency sputtering.

2.1.1.2 Pulsed DC sputtering

For pulsed DC sputtering, the DC power supply in Figure 4 is replaced by a pulsed DC power supply. This pulse is asymmetric in time and periodically changes the polarity of the target. During the negative pulse, positive ions are attracted to the target; during the positive pulse, electrons are attracted to the target.

2.1.1.3 RF sputtering

In this arrangement, the DC power supply in Figure 4 is replaced by an RF power supply. (See Figure 5.)

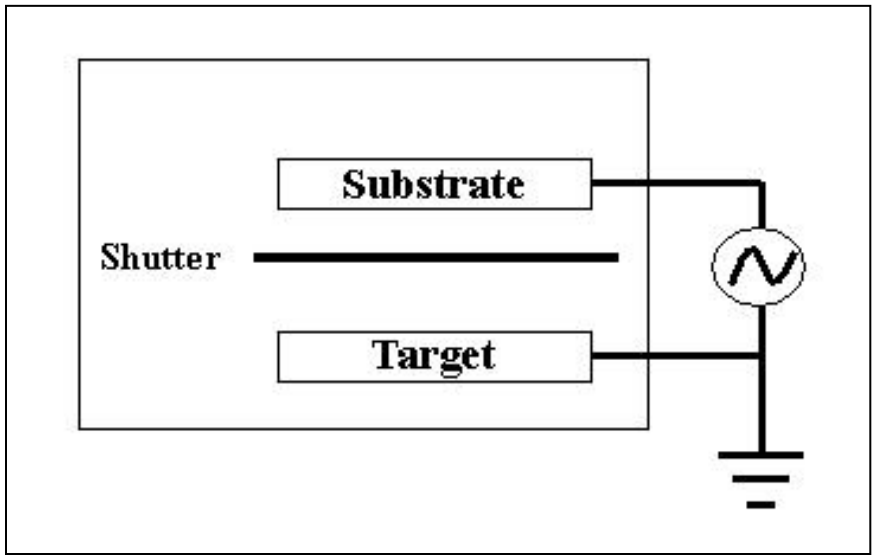

Figure 5. Schematic of RF sputtering

RF sputtering is generally performed at 13.56 MHz. At this frequency, massive ions cannot follow the temporal variations in the applied potential, but the electrons can. In a balanced system, both electrodes are configured as identical sputtering targets, and their potentials are 180^{o} out of phase. By alternating the polarity of the target electrode, net charge build up can be eliminated. As a result, RF sputtering can be used to deposit electrically conducting, semi conducting, and insulating coatings. Also, the high frequency plasma oscillations enhance the ionization rate, so the RF sputtering system can be operated at considerably lower pressures than DC discharges.

2.1.1.4 Magnetron sputtering

To confine the plasma to a region near the target surface, a set of permanent magnets is placed under the target. Figure 6 shows the schematic of a circular planar magnetron.

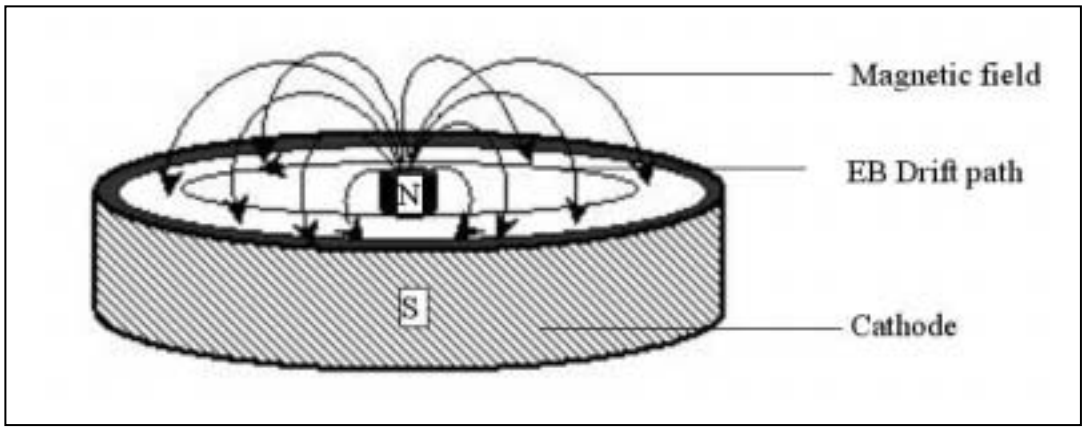

Figure 6. A circular planar magnetron

The central axis is one pole, and an annular ring at the edge is another. The magnetic field lines travel from the central pole to the outer ring. The electric field points in the upper direction. An electron undergoes a drift motion in combined electric and magnetic fields. This motion, known as EB drift, is in a direction perpendicular to both the electrical and the magnetic fields. The EB drift is approximately parallel to the surface of the cathode and forms a closed path. The secondary electrons emitted from the cathode surface are approximately constrained in this annular region, resulting in increased ionization and much denser plasma. Magnetron sputtering can be used for both DC and RF sputtering.

2.1.2 Sputtering modes

There are two primary modes for the formation of sputter deposited films: non-reactive and reactive sputtering.

For non-reactive sputtering, the inert gas, usually Ar, does not participate directly in the formation of compounds on either the target or substrate.

For reactive sputtering, other inert gases like oxygen or nitrogen are fed into the sputter chamber in addition to the argon to produce oxide or nitride films. The inert gas can have a chemical reaction with the target or substrate. Reactive sputtering can be used together with all four sputtering techniques described above.

In our experiment, AlFe films are deposited using non-reactive DC magnetron sputtering. AlN films are deposited using reactive pulsed DC magnetron sputtering.

2.1.3 Sputtering equipment

The Kurt J. Lesker Super system is utilized as the deposition tool for this work. Three valves separate the machine into four chambers: the main vacuum chamber, the load-lock chamber, and two cryopump chambers, one of which is 8 inches in diameter and the other 12 inches. The load-lock chamber which is utilized to load a substrate before deposition separates the main vacuum chamber from all contamination. Sputtering deposition takes place in the main vacuum chamber, a cylinder with a diameter of approximately 1 meter and a height of approximately 60 cm. Up to four targets can be inserted into the base plate of the main chamber. An aperture ensures that only one target at a time can be used for deposition which prevents the other targets from being coated.

Two kinds of targets were used in our experiments: one is aluminium (20 cm in diameter) and the other is iron/aluminium alloy (82.3/17.5 WT%, 4.00 Inch DIA, 0.080 Inch Thick, 99.99% purity). In general, under the target, there is a circular magnetron which traps electrons in cycloids which then circulate over the target surface. Substrates are either flat disks or small cylindrical rods. They are cleaned using 75% IPA alcohol before deposition and then are mounted on the substrate holder. The substrate holder is attached to the top cover opposite to the target. The substrate-target distance is 13-17 cm,

and it can be adjusted under computer control. Ar and nitrogen gas can be input into the main chamber from gas invents. Nitrogen is utilized to induce a reaction between the target material and nitrogen to form nitride films. This system is schematically shown in Figure 7.

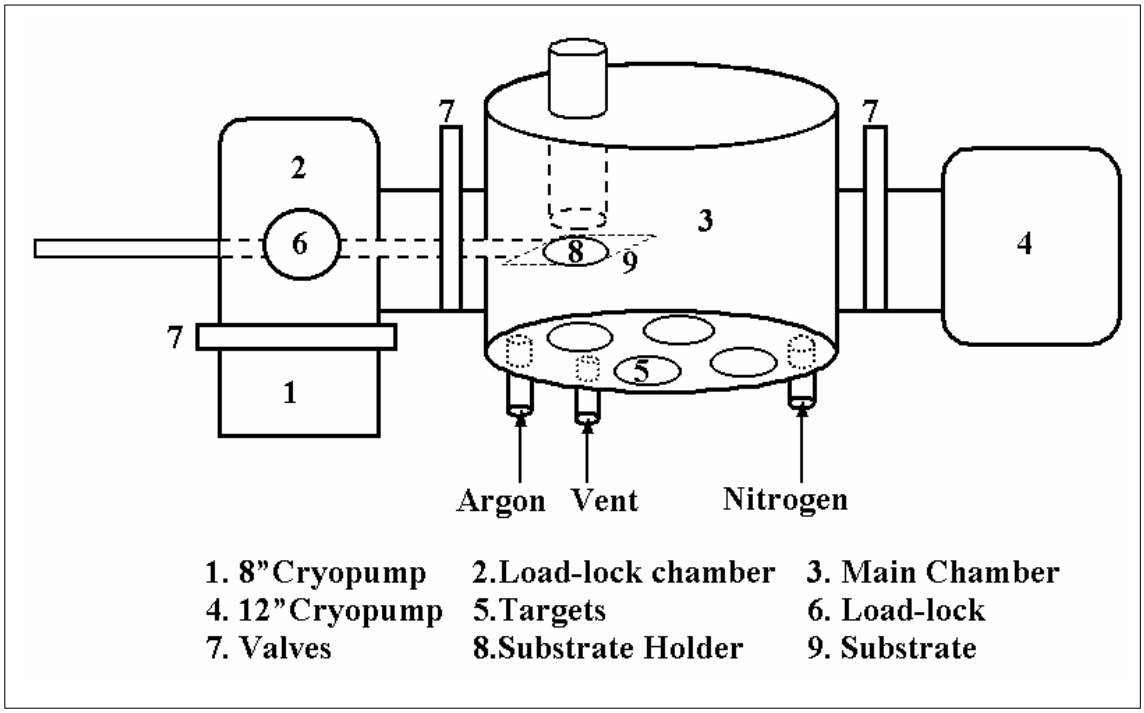

Figure 7. Schematic of the sputtering machine

The basics of the sputtering system used in this study are summarized in Table I.

Table I. Summary for Sputtering

Name	**Type**
Power	DC/Pulsed DC
Inert gas	Ar, Ar+N_2
Target	Al, AlFe alloy
Substrate	Silicon wafer, Aluminium rod
Thin films	Al, AlFe, AlN, AlFeN

2.1.4 Sputtering Deposition Parameters

When depositing the desired material, several experimental parameters are monitored. The film properties can be controlled by adjusting the following sputtering parameters:

Sputter current -- determines mainly the rate of deposition.

Applied voltage -- determines the maximum energy with which sputtered particles can escape from the target.

Pressure in the main chamber -- determines the mean free path for the sputtered material.

2.1.5 Sputtering Deposition Process

In our experiment, AlFe films are produced in a non-reactive DC magnetron process. The base pressure of the main chamber is approximately 4 μtorr . The argon flow rate is fixed at approximately 25 sccm (standard cubic centimetres) to raise the deposition pressure to 2.8 mtorr . A DC power (200 watt) is applied to the cathode and anode. A voltage potential of approximately 300 is set up between the electrodes.

AlN and AlFeN films are produced in a reactive pulsed-DC magnetron sputter process. The base pressure is set at a lower level (1.0~1.5 μtorr). The argon flow rate is fixed at 20 sccm. Besides argon, nitrogen is added into the main chamber with a flow rate of about 18~23 sccm; thus the deposition pressure of the main chamber is about 3.5 mtorr . A pulsed DC power (500~2000 watt) is supplied to the electrodes. The deposition voltage/current is 202/10.14 for AlN and 270/1.92 for AlFeN. The sputtering deposition parameters in our experiments are listed in Table II.

Table II. Parameters for the Sputtering Deposition

Parameter	AlFe	AlN	AlFeN
Base Pressure (μ Torr)	3.2	1.0	1.5
Argon (sccm)	25	20	20
Nitrogen (sccm)	0	18	23
Pressure (mTorr)	2.82	3.38	3.65
Power (watt)	200	2000	500
Voltage (volt)	323	202	270
Amps (amp)	68	10.14	1.92
Deposition Time (minute)	5	15	15

2.2 Thin film characterization

2.2.1 Thin film analytic methods

There are lots of techniques used for thin film chemical and physical analysis, each of which provides a substantial amount of information. To obtain the optimum information, it is often benificial to combine several techniques.

In this paper, Scanning Electron Microscopy (SEM), Energy Dispersive Spectropy (EDS), Atomic Force Microstropy (AFM) and X-ray diffraction (XRD) are used to analyze the properties of the AlFe and AlN films. EDS is used to get the element percentage of the film. AFM is used to characterize the morphology of thin films. Film thickness is obtained from SEM. Crystal structure is revealed via XRD[6].

2.2.2 Thickness

Film thickness is examined via SEM. One of the SEM cross-section images of AlFe film on a silicon wafer is illustrated in Figure 8. We can see that there are two parallel dotted lines. The region between them is the thin film layer; the upper line is X, which is set at 0; and the lower dotted line is Y. The region below Y is the silicon wafer. The distance between X and Y is D, which represents the thickness of the film. A few

AlFe films coated on silicon wafer were measured by SEM. The AlFe film thickness has a range from 130nm to 2 um.

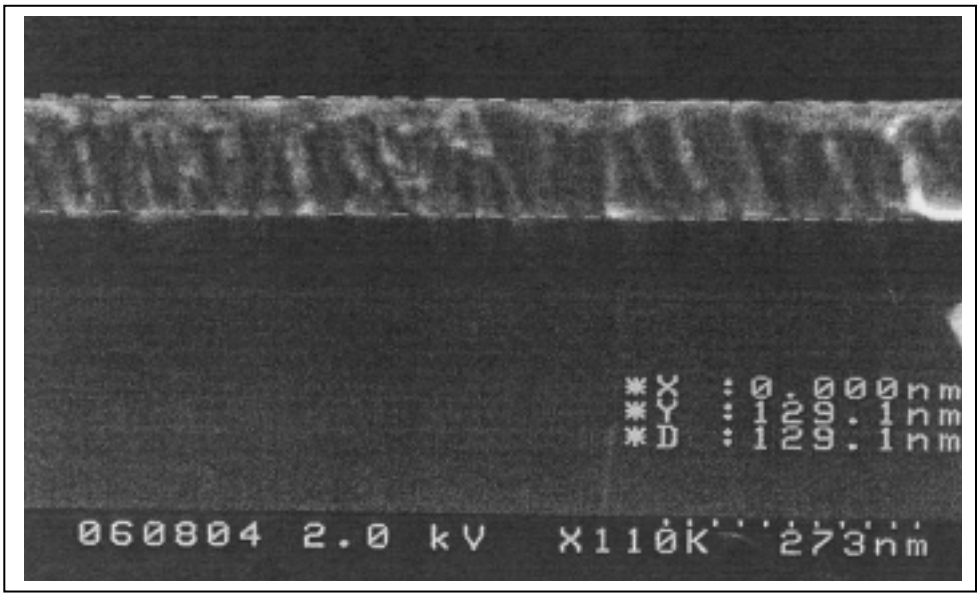

Figure 8. SEM analysis of AlFe film on silicon wafer

Figure 9 illustrates the SEM cross-section image of AlN.

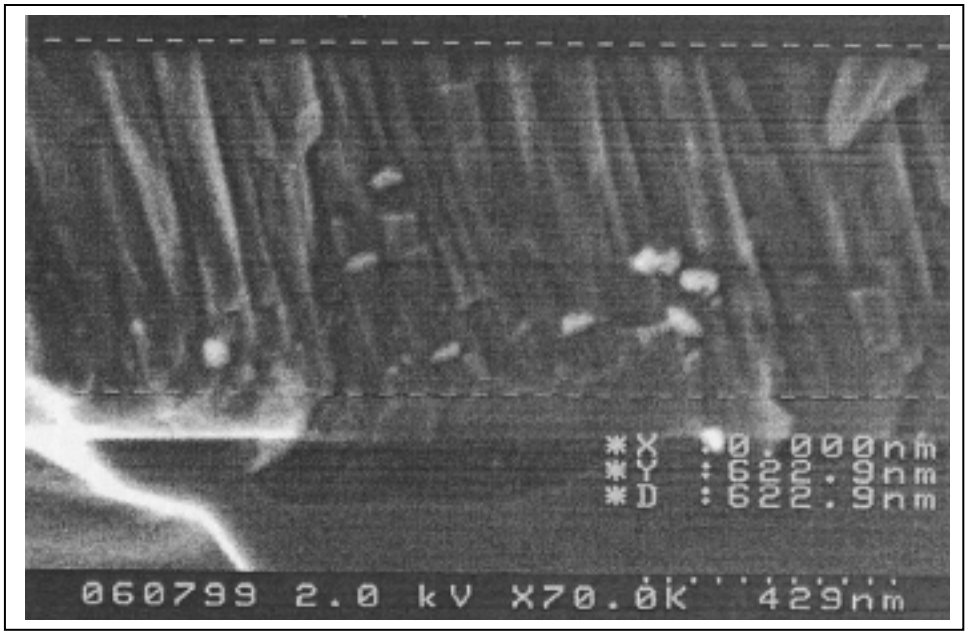

Figure 9. SEM analysis of AlN film on silicon wafer

From the SEM image of AlN, we can see that the AlN film growth appears to be in columns. The average thickness of AlN film is 695nm. The thickness of these films is summarized in Table III.

Table III. Thin Film Thickness

Thin film	AlFe	AlN
Thickness	130nm~2um	695nm

2.2.3 Roughness of AlN films

The roughness of AlN films is analyzed by AFM. Figure 10 shows the roughness result of aluminium nitride film analyzed by AFM.

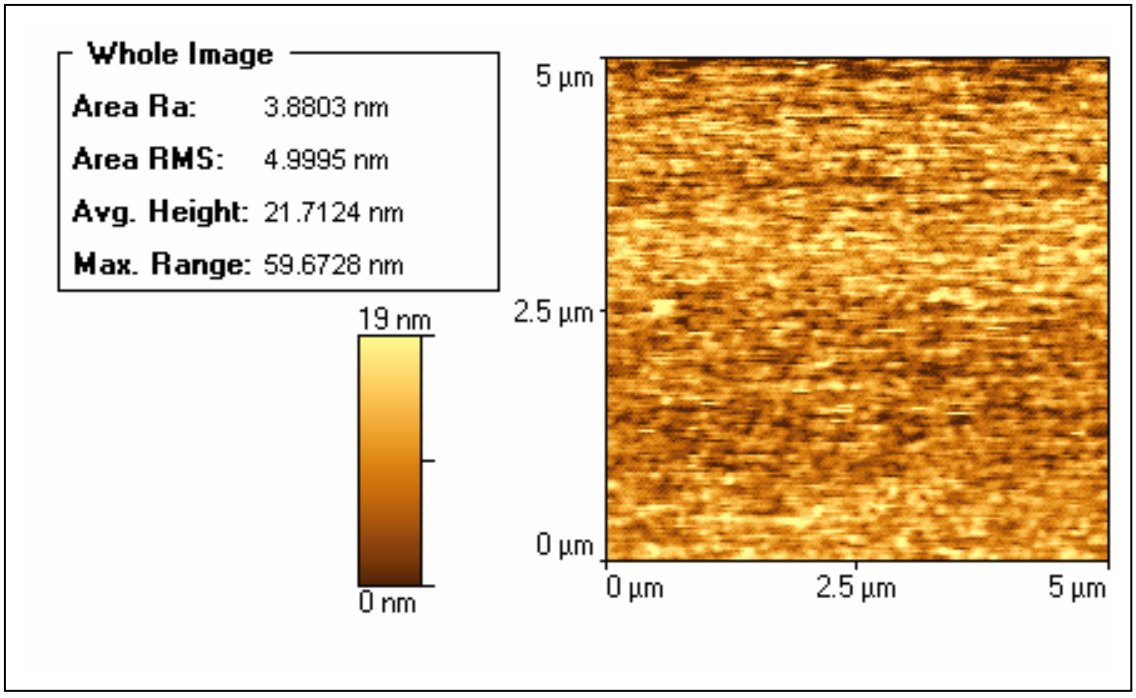

Figure 10. Roughness of AlN film

The roughness results are reported as four values:

Average roughness (Ra)——The average surface roughness of average deviation of all points from a plane fit to the test part surface.

Root mean square roughness (RMS)——The root-mean-square average of the mearsured height deviations taken within the evaluation length or area and measured from the mean linear surface.

Average height——Average height for the scanning sample surface.

Maximum range——Maximum peak to valley height over the sample.

Three samples were taken from the top, center, and bottom parts of the film. The average roughness for AlN films according to AFM is about 4nm, as tabulated in Table IV.

Table IV. AlN Film Roughness by AFM Analysis

Film	**Sample**	**Ra(*nm*)**	**Rms(*nm*)**	**Average Height (*nm*)**	**Maximum Height (*nm*)**
AlN	Top	4.0007	6.0047	20.8262	134.4116
	Center	4.2761	5.4303	24.0759	53.7646
	Bottom	3.8803	4.9995	21.7124	59.6728
	Average Value	4.0524	5.4782	22.2048	82.623

2.2.4 XRD patterns of AlN and AlFe film

Figure 11 is the x-ray diffraction pattern of AlFe film. Two peaks can be seen, peak #1 is a sharp peak and peak #2 is a board peak. No peak can be found in PDF which matches peak #1. However, in the range of the board peak, many PDF peaks can be found, there are aluminum iron, aluminum oxide and iron (JCPDS PDF # 45-1203, 45-0983, 45-0982, 39-0824, 33-0020, 06-0696).

Figure 12 is the x-ray diffraction pattern of the AlN film. There are 8 peaks. Peaks 1 and 6 are sharp peaks, and no peaks in PDF can be found to match these two peaks. Peaks 2, 3, 4, and 5 are board peaks which match very well with the peaks in the PDF of aluminum nitride (JCPDS PDF # 25-1133). This result indicates that an aluminum nitride phase is present.

The XRD analysis for AlFe and AlN were repeated; a sharp peak appears in every pattern and at the same location, which shows that it is just a spark and not related to any elements or compounds.

Crystallite sizes based on XRD patterns were calculated. The results show that the crystallite size for AlFe is about 7nm and about 13.5nm for AlN.

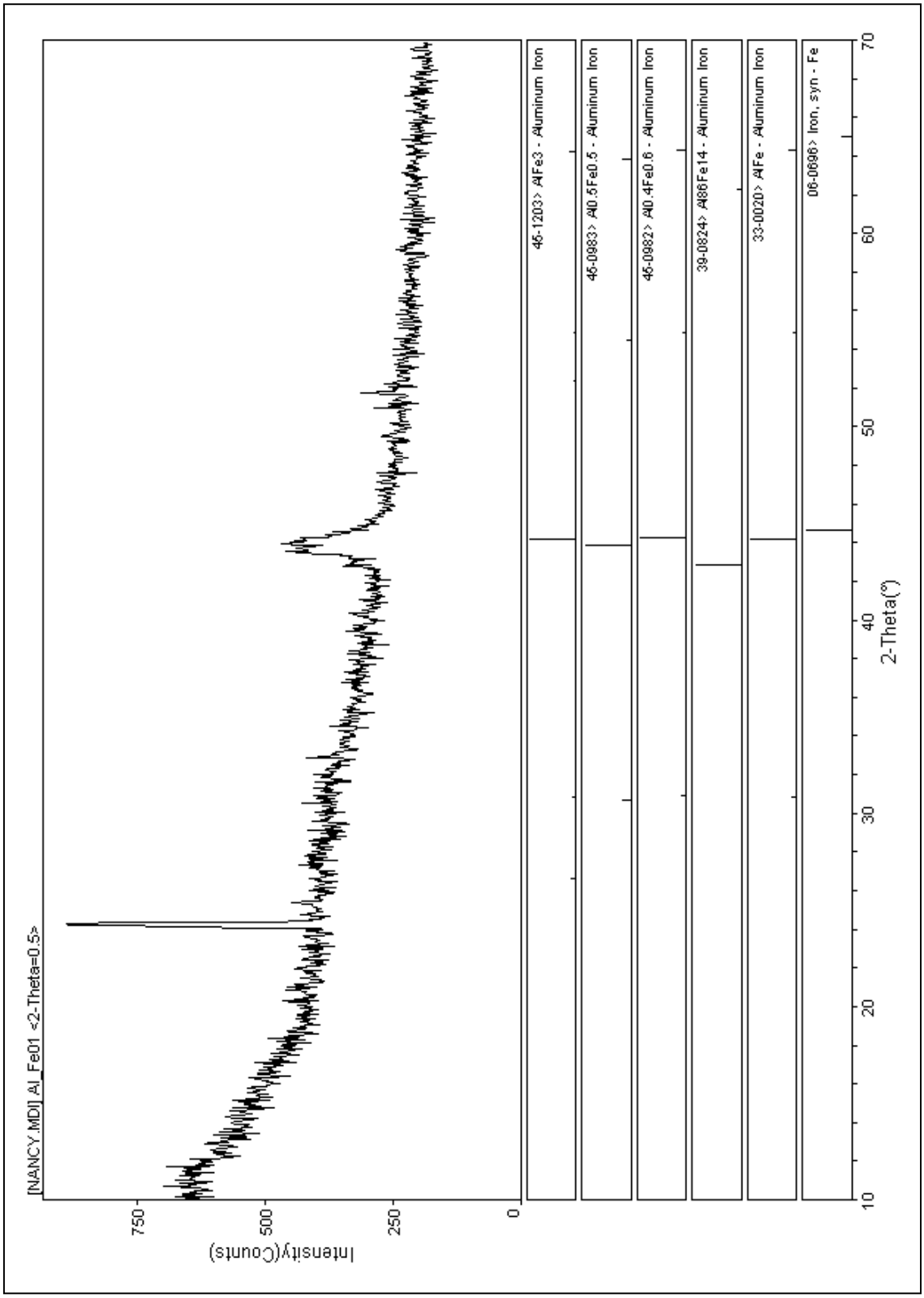

Figure 11. XRD analysis of AlFe film

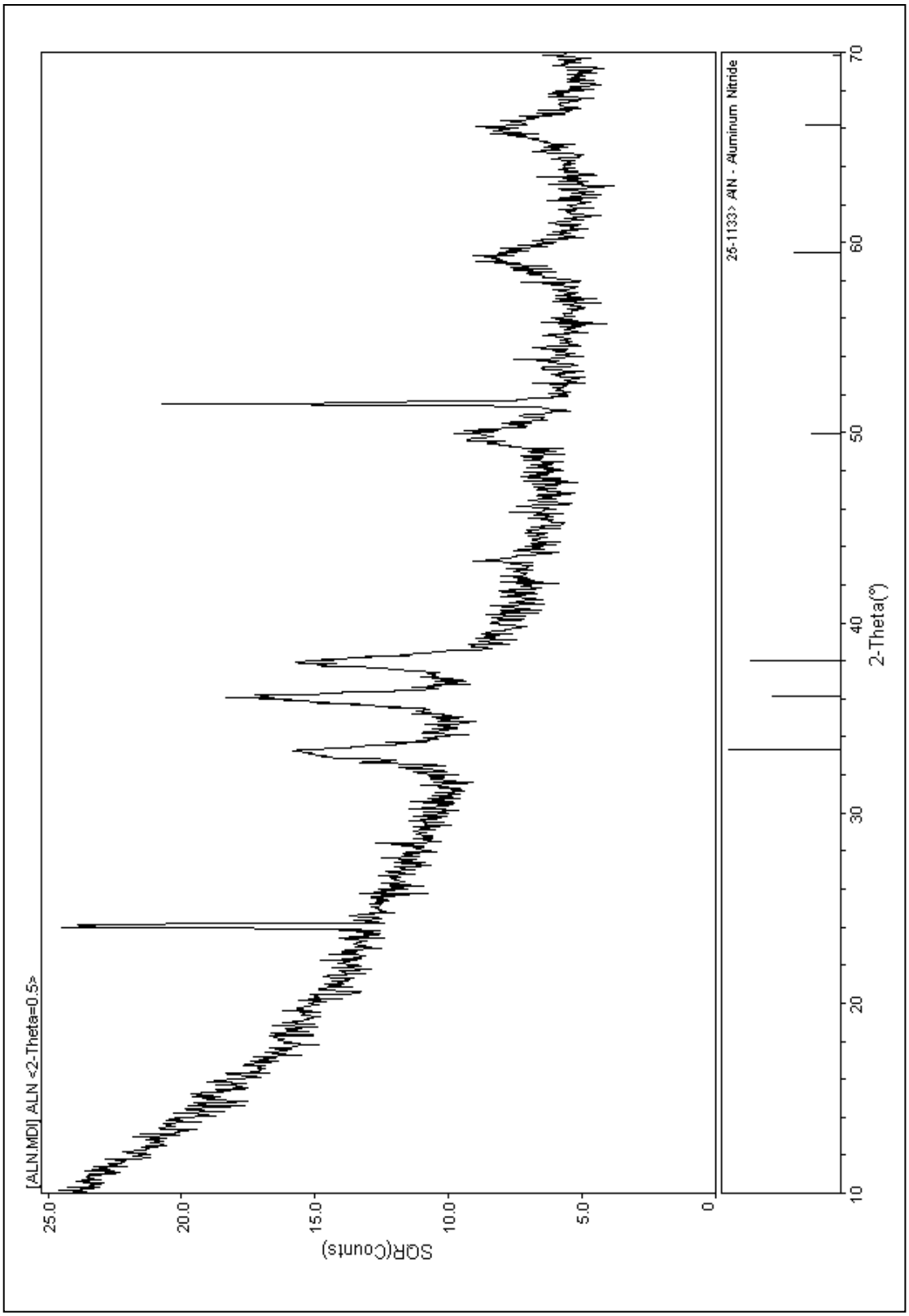

Figure 12. XRD analysis of AlN film

2.2.5 Energy dispersive X-ray analysis of AlFe film

Energy dispersive X-ray analysis of AlFe is illustrated in Figure 13. It shows the elemental mapping of AlFe film on the silicon wafer. In addition to aluminum and iron, oxygen is present on the film surface, which is consistent with the XRD result.

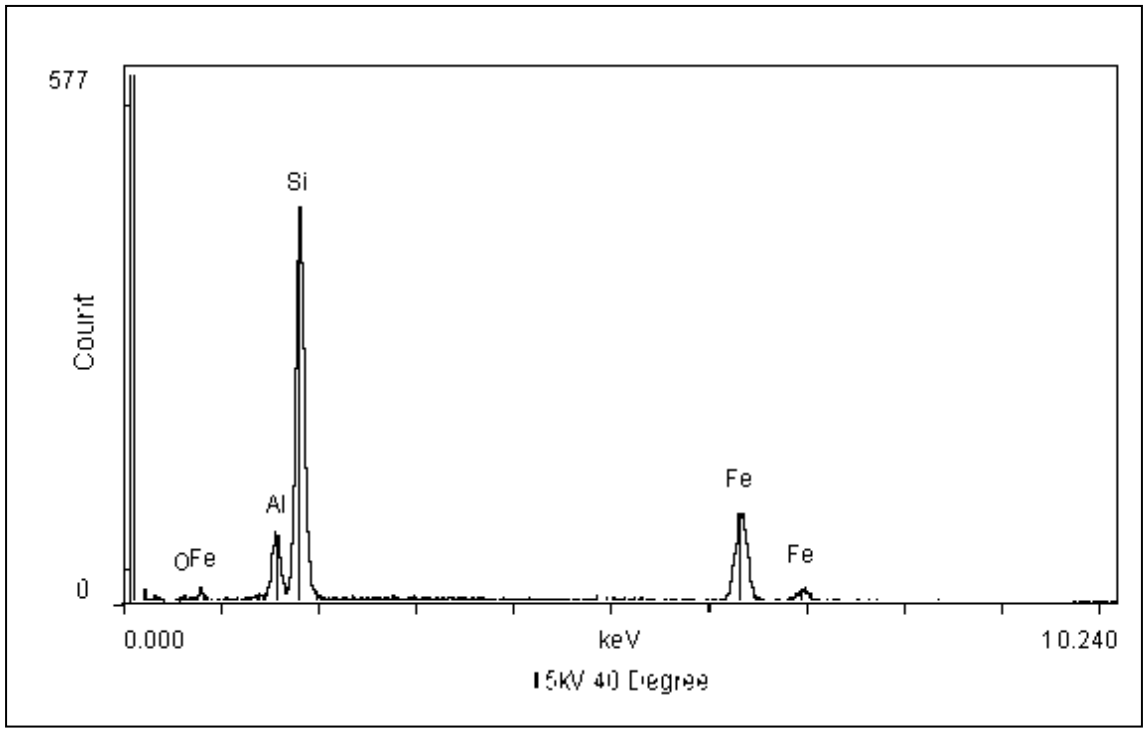

Figure 13. Elemental Mapping of AlFe Film on silicon wafer

In the AlFe alloy target, the aluminum weight percentage is 17.5%, and the iron weight percentage is 82.3%. After magnetic sputtering deposition, the element weight percentage of the as-deposited AlFe film on the silicon wafer is as follows: Al 42.1 wt%, Fe 57.9 wt%. (See Table V for comparison.)

Table V. Element Weight Percentage after Deposition

Element	Original target (WT%)	AlFe film on silicon wafer.
Al	17.5	42.1
Fe	82.3	57.9

2.2.6 Electrical conductivity of AlFe film

The electrical resistance of the 129nm AlFe film is 80 ohm, which is measured using

an ohmmeter.

The electrical conductivity of the shielding material is the necessary input for the Maxwell 2D eddy current solver. In the following, we calculate the electrical conductivity of AlFe film from the measured resistance:

The conductivity, G is given by,

$$\mathrm{G} = \frac{1}{\rho} \tag{2-1}$$

where ρ is resistivity, it is defined as,

$$\rho = \frac{R \times A}{L} \tag{2-2}$$

where R resistance, A is the area of thin film cross section , L is length

$$A = W \times H \tag{2-3}$$

$$\mathrm{G} = \frac{1}{\rho} = \frac{L}{R \times A} = \frac{L}{R \times W \times H} \tag{2-4}$$

where W is the width, H is the thickness of the film. Shown in Figure 14.

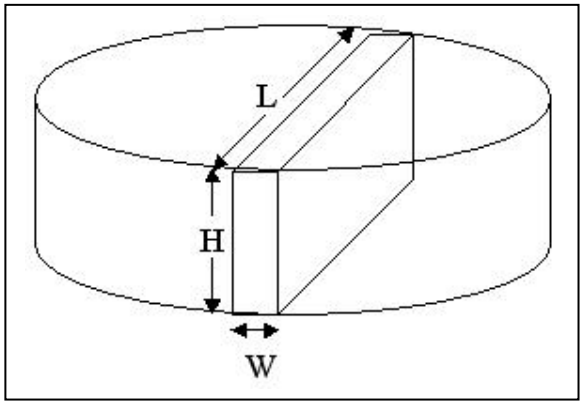

Figure 14. Conductivity of AlFe film on silicon wafer

The conductivity of the 129nm AlFe film can be calculated as:

$R = 80\,\Omega$

$H = 129\text{nm} = 1.29 \times 10^{-7}\,\text{m}$

L = diameter of silicon wafer = 6 inch = 0.1524m

$W = \frac{1}{2} \times \text{diameter of silicon wafer} = \frac{1}{2} \times 6\,\text{inch} = 7.62 \times 10^{-2}\,\text{m}$

$$G = \frac{1}{\rho} = \frac{L}{R \times W \times H} = \frac{0.1524}{80 \times 7.62 \times 10^{-2} \times 1.29 \times 10^{7}} = 1.92 \times 10^{4}\ \text{siemens/meter}$$

The conductivity of the 129nm AlFe film is 1.92×10^{4} siemens/meter.

2.2.7 Film stress

Due to the difference between the expansion coefficients of the film and substrate or due to strains developed during the growth process, films and coatings on substrates may have a residual stress that is either compressive or tensile. These stresses contribute to adhesion failure.

Film under compression will try to expand, and if the substrate is thin, then the film will bow the substrate on the convex side. If the film has a tensile stress, the film is on the concave side. Tensile stress may be relieved by micro cracking the film. The film stress may not be uniform throughout the film thickness, and there may be a stress gradient in the deposit. The film stress is tabulated in Table VI.

Table VI. Thin Film Stress

Thin film	AlFe	AlN	AlFeN
Stress ($Dyne/cm^2C$)	-7.080×10^{8}	2.852×10^{9}	-3.42×10^{9}

From Table VI, we can see that the AlN film stress is opposite to that of AlFe and AlFeN film. Presumably, when AlN film is stacked next to AlFe film, the combined stress is lower than that of each film individually.

2.2.8 Magnetic permeability

2.2.8.1 Hysteresis loop

Materials can be classified into diamagnetic, paramagnetic, ferromagnetic, ferrite, and anti-ferromagnetic materials according to their magnetic properties. Their magnetization curves are shown in Figure 15, where the magnetic field strength is plotted along the horizontal axis and the magnetic flux density along the vertical axis.

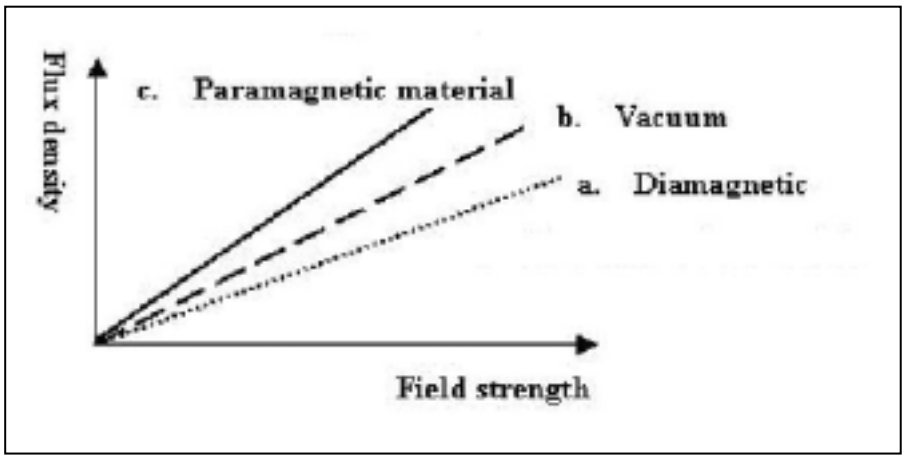

Figure 15. Magnetization in different materials

As Figure 15 shows, Line b, the curve in a vacuum, is linear, and the gradient of the curve corresponds to the permeability. Line a, the curve for diamagnetic material, shows that its flux density grows slightly more slowly than Line b does. Line c, the curve for paramagnetic material, shows that its flux density grows slightly faster than Line b does.

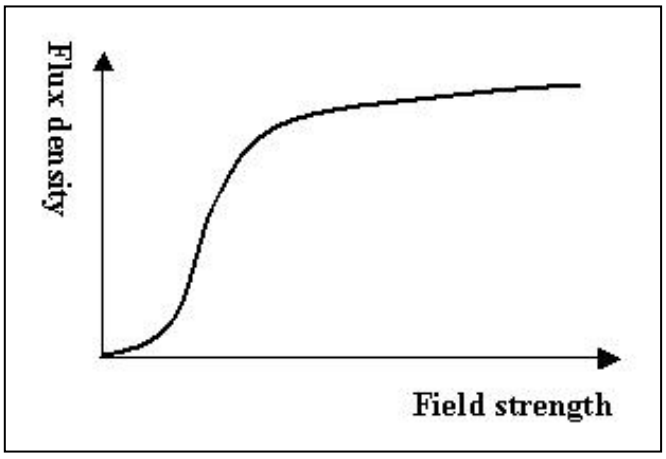

Figure 16. Magnetization of ferromagnetic material

The curve in Figure 16 is the initial magnetization of ferromagnetic material. Ferromagnetic material is distinguished from diamagnetic and paramagnetic material not only by permeability but also by remanence and coercivity. According to the coercivity, the material can be classified as "hard" and "soft"magnets. For "hard" magnets, the coercivity is so large that the material keeps its magnetization once it is magnetized. Hard magnetic materials can generate a magnetic flux density in the air gap of a magnetic device without any external power supply. For soft magnetic materials, the coercivity (Hc) is small so that it can only keep a substantial magnetization with the aid of an externally applied magnetic field. Figure 17 shows a hysteresis loop for a typical hard magnetic material.

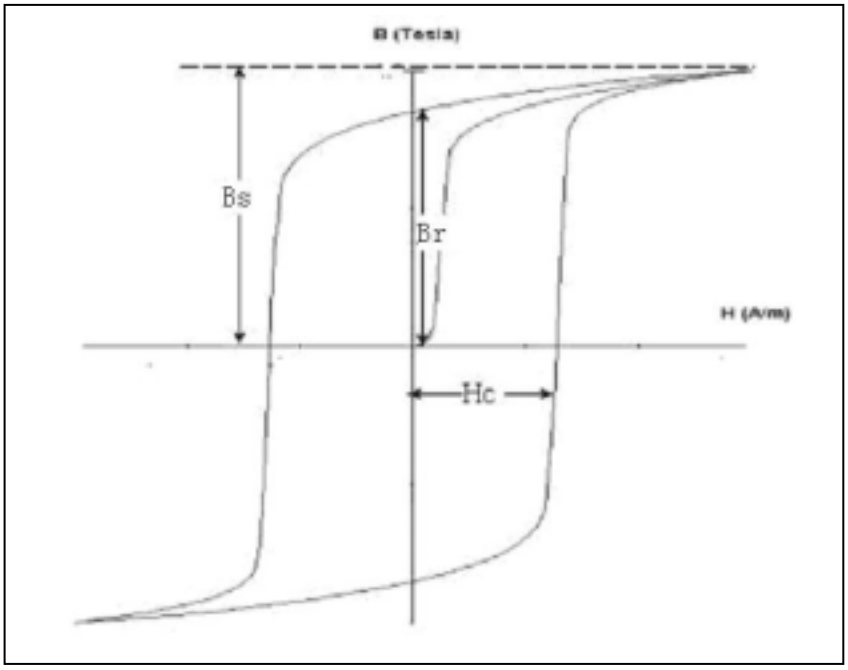

Figure 17. A hysteresis loop for a typical hard magnetic material

Figure 17 shows that as the magnetic field H increases from zero, the sample, which was initially non-magnetized, starts to magnetize and follows the initial magnetization curve in the first quadrant of the B-H plane. When the magnetic field is strong enough to saturate the magnetic moments of the magnetic material, the magnitude of the magnetization reaches its saturation magnetization Ms. When the applied magnetic field H is reduced back to zero, the magnetization M and the magnetic induction B do not return to zero. B and M still have finite values which are called the remanent magnetic

induction, B_R and remanent magnetization M_R. In order to make the magnitude of B return to zero, the direction of the applied magnetic field H should be opposite to that of the initially applied magnetic field direction. The magnitude of the opposing applied magnetic field which makes the magnetic induction zero is called the coercivity, H_c, when B (H_c)=0. By varying the applied magnetic field H over one entire cycle, the hysteresis loop is obtained.

Figure 18 shows the hysteresis loop for a typical soft magnetic material.

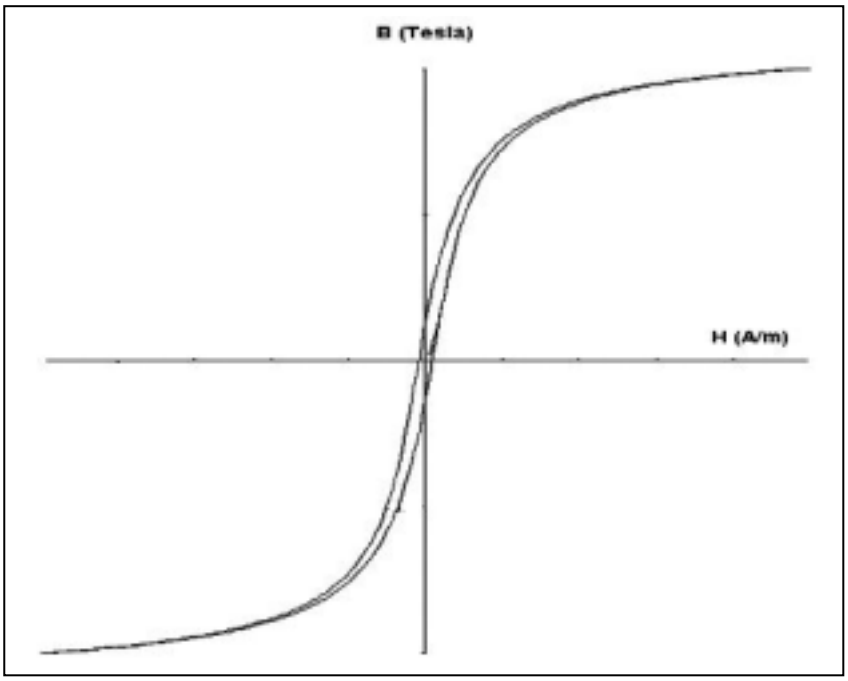

Figure 18. A hysteresis loop for a typical soft magnetic material

The coercivity for the soft magnetic material is quite small compared to that of hard magnetic material, and the hysteresis loop is much narrower.

2.2.8.2 Magnetic properties for AlFe films

The AlFe film is used as the shielding material, which will work in the 64MHz magnetic field, so it is very important to obtain the high frequency magnetic properties of AlFe.

The hysteresis loops for AlFe films with a thickness of 500nm and 150nm are illustrated in Figure 19 and Figure 20 respectively. These loops are measured with Vibrational Sample Magneto-meter (VSM) at 300K. Data were recorded at magnetic field increments of 0.5 milliOe near the field origin. Values for the saturation magnetic

moment Ms, remanence magnetic moment M_r, coercivity H_c, and squareness ratio (SQR) are tabulated in Table VII.

In Figure 19, a hysteresis loop measured with VSM at 300K for an AlFe film with a thickness approximately 500nm is illustrated. The loop appears to have two sections. One section is in the region between plus and minus 100 oested, which has a certain squareness similar to that illustrated in Figure 18 for a thinner film. The other section is either between 100 oested and 400 oested or between -100 oested and -400 oested, which may indicate that the effective magnetic moment in the top portion of the film is not aligned in the plane of the substrate.

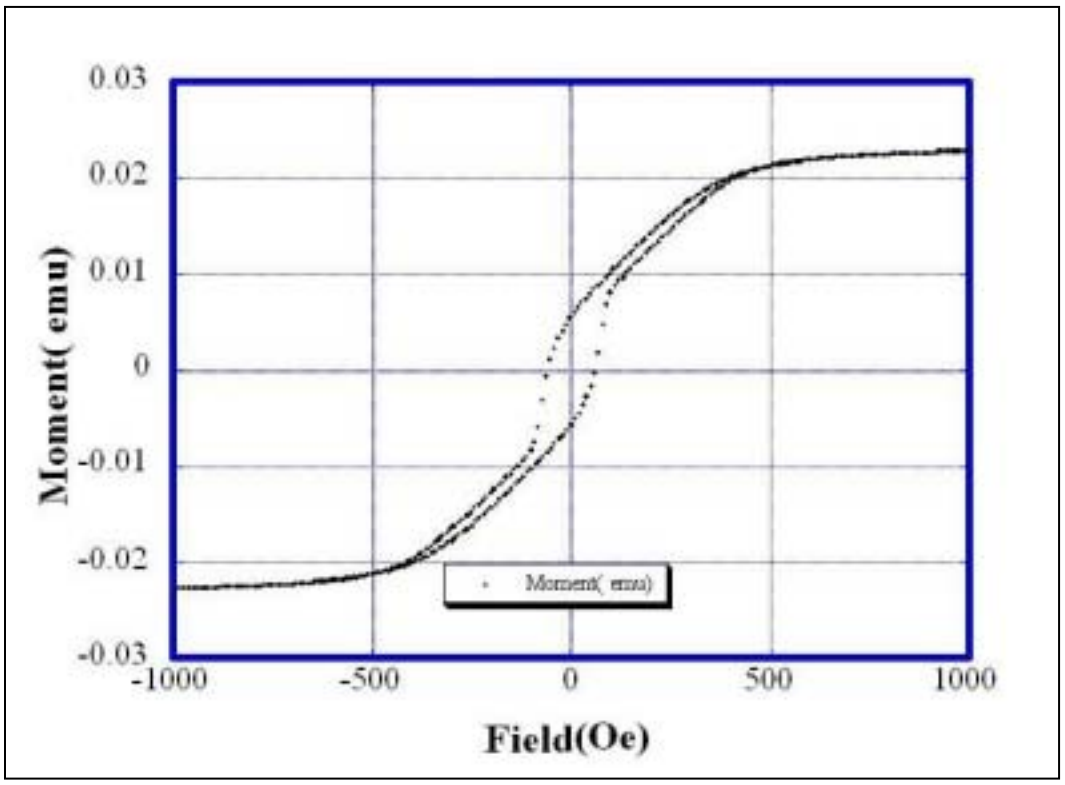

Figure 19. Hysteresis loop for a FeAl film with a thickness of approximately 500nm

The saturation magnetic moment is approximately 0.02 emu. The effective anisotropy field is approximately 400 Oested.

The size of the sample is $6\text{mm} \times 5\text{mm}$, so the volume for the 500nm AlFe film is:

$$V_{500} = 1.5 \times 10^{-5}\,\text{cm}^3 \tag{2-5}$$

It is well known that,

$$1\mathrm{Am}^2 = 10^3\,\mathrm{emu} \tag{2-6}$$

$$1\mathrm{Am}^{-1} = 4\pi \times 10^{-3}\,\mathrm{Oe} \tag{2-7}$$

$$1\mathrm{emu} = 4\pi\mathrm{Oe}\cdot\mathrm{cm}^3 \tag{2-8}$$

The saturation of magnetization of the 500nm AlFe is,

$$\mathrm{M_s} = \frac{0.002 \times 4\pi \times \mathrm{Oe}\cdot\mathrm{cm}^3}{1.5 \times 10^{-5}\,\mathrm{cm}^3} = 16746\mathrm{Oe} \tag{2-9}$$

The magnetic permeability of AlFe film is calculated as:

$$\mu = \frac{\mathrm{M_s}}{\mathrm{H_c}} = \frac{16746\mathrm{Oe}}{400\mathrm{Oe}} = 41 \tag{2-10}$$

For the AlFe film with a thickness of approximately 150nm, a magnetic hysteresis loop measured with VSM at 300K is illustrated in Figure 20.

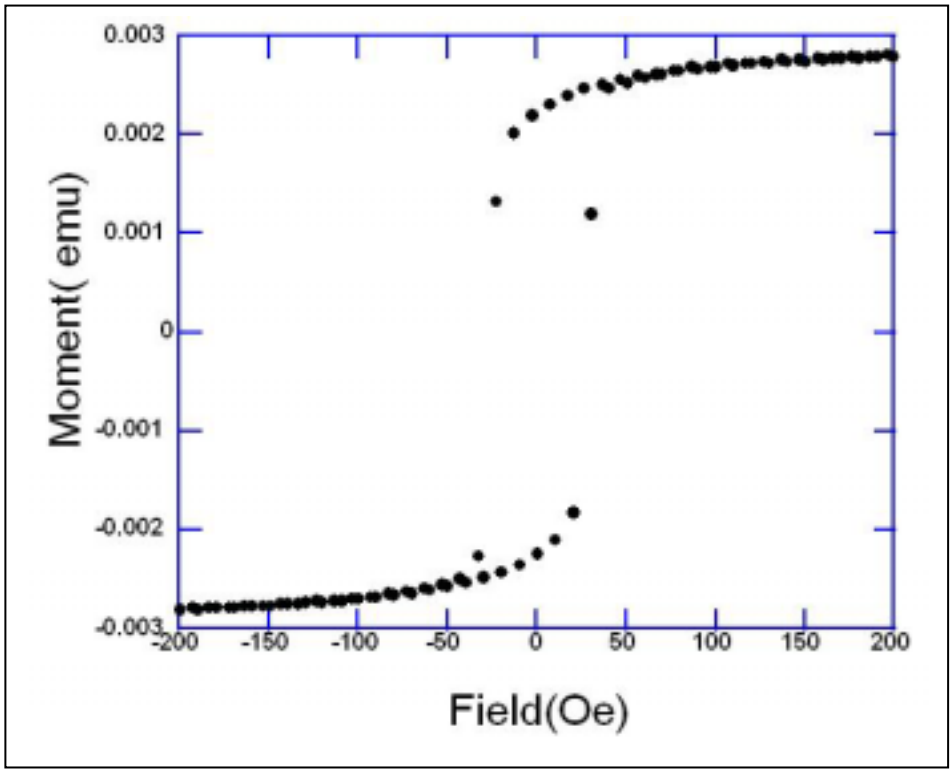

Figure 20. Hysteresis loop for a FeAl film with a thickness of approximately 150nm

The coercivity Hc is approximately 50 Oested, the remanence magnetic moment is approximately 0.0022 emu, and the saturation magnetic moment is approximately 0.0025 emu.

The squareness of the loop, given by,

$$SQR = M_r / M_s \tag{2-11}$$

is approximately 80%.

The initial magnetic permeability can be calculated from:

$$\mu = \frac{B}{H} \tag{2-12}$$

The size of the sample is $6mm \times 5mm$, so the volume for the 150nm AlFe film is:

$$V_{150} = 4.5 \times 10^{-6} cm^3 \tag{2-13}$$

Correspondingly, the maximum magnetic field strength is,

$$B_s = \frac{0.0025 \times 4\pi \times Oe \cdot cm^3}{4.5 \times 10^{-6} cm^3} = 6977Oe \tag{2-14}$$

The initial magnetic permeability of the 150nm AlFe film is calculated from:

$$\mu = \frac{B}{H} = \frac{6977}{50} = 138 \tag{2-15}$$

The magnetic properties of aluminum ion at 64MHz are tabulated as:

Table VII. Magnetic Properties of AlFe

	m_s(emu)	M_s (Oested)	H_c (Oested)	SQR	μ
500nm AlFe	0.02	16746	400	/	41
150nm AlFe	0.0025	6977	50	0.8	138

2.2.9 Energy distribution in thin films

Shielding is based on two major electromagnetic phenomena: reflection and absorption. It is very important to measure the energy distribution when the electromagnetic wave strikes the AlFe and AlFeN films.

The results for the AlFe and AlFeN films coated on a silicon wafer at 64MHz were tested at SUNY Buffalo. They are shown in Table VIII.

Table VIII. Transmission and Reflection (dB) in the Films

SE	129nm AlFe	623nm AlFeN
Transmission (dB)	-18.8 ± 0.2	-29.2 ± 0.1
Reflection (dB)	-1.3 ± 0.1	-0.7 ± 0.1

Since we know that

$$SE(dB) = 20\log\frac{V_1}{V} \tag{2-16}$$

then the percentage of the energy distribution (transmission, reflection, and absorption) in the thin film coated wafer can be calculated as:

$$\frac{V_1}{V}\% = 10^{\frac{SE}{20}}\% \tag{2-17}$$

The percentage of the absorption energy is calculated as one hundred percent minus the percentage of transmission and reflection energies. These energy distribution results for the uncoated silicon wafer and the thin film coated wafer are listed in Table IX.

Table IX. Energy Distribution Comparison between the Uncoated and Coated Wafer

	129nm AlFe		623nm AlFeN	
Percentage	Uncoated wafer	Coated wafer	Uncoated wafer	Coated wafer
Transmission (%)	57.14	10.96	56.89	3.47
Reflection (%)	38.90	84.14	38.90	92.26
Absorption (%)	3.96	4.9	4.21	4.61

From the above Table, we can see that after coating, the reflected power increases a lot. Very little power is transmitted and absorbed.

3 Magnetic shielding computer simulation.

3.1 Shield basics

Magnetic shielding: Preventing the magnetic field from affecting a device is called magnetic shielding.[7]

As Figure 21 shows, an electromagnetic wave striking a shell surface results in two kinds of losses: reflection and absorption.

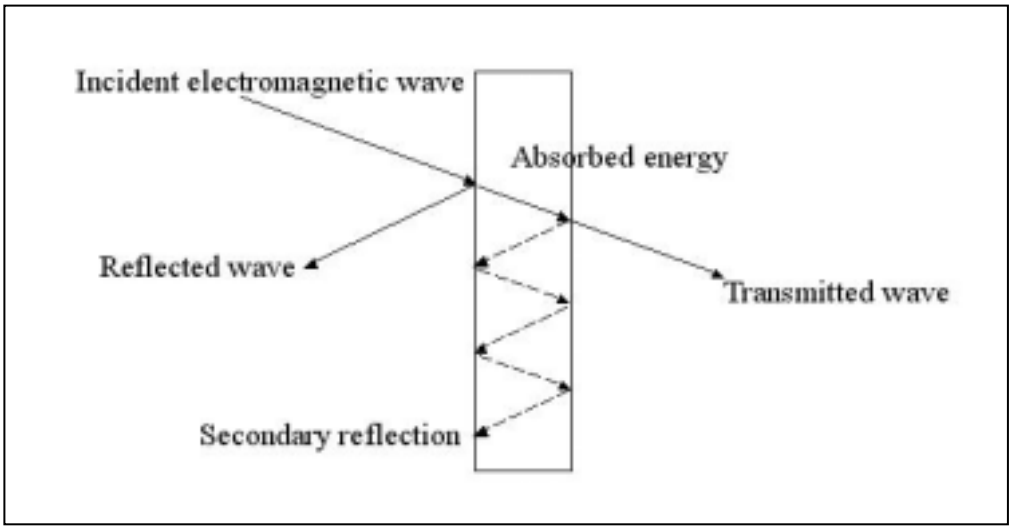

Figure 21. Shield attenuation of electromagnetic wave

Part of the wave is reflected while the remainder is transmitted and attenuated as it passes through the shell. The combined effect of these losses determines the effectiveness of the shield. Absorption is the transformation of the wave energy in the shield to heat. The attenuation in the shield is described by,

$$A_{db} = \frac{8.68t}{\delta} \tag{3-1}$$

where t is the thickness of the shielding material and δ is the skin depth. Skin depth is defined as:

$$\delta = \sqrt{\frac{1}{\pi f \mu_r \mu_0 \sigma}} \tag{3-2}$$

where δ is skin depth in meter, μ_r is the relative permeability, μ_0 is the permeability of free space, which is equal to $4\pi \times 10^{-7}$ Henry/meter, σ is the conductivity of conductor in siemens/meter.[8] From the above formulas, we can see that the skin depth does the following:

Decreases with an increase in frequency

Decreases with an increase in conductivity

Decreases with an increase in permeability

For a single layer shielding, the degree of shielding effect can be represented as shielding factor (SF), which is the ratio between the unperturbed magnetic field Bo and the shielded magnetic field Bi as expressed as:

$$SF = \frac{B_i}{B_o} \tag{3-3}$$

The final shielding design depends on the following critical factors: maximum predicted magnetic field intensity, shield geometry, and shielding material properties of conductivity and permeability.

3.2 Computer simulation

The purpose of this study is to use thin film magnetic shielding to solve the heating problem in the electrical wire under MRI procedure. The shielding effect will vary according to the properties of the shielding material. These material properties are affected during the sputtering deposition process. To get the exact temperature in the electrical wire, a vivo mode is set up. A lot of experiments may be necessary to get the optimal shielding effect. So it is meaningful to do computer simulation before the vivo experiments in order to save money, time, and effort.

3.2.1 Maxwell equations and Maxwell 2D

Maxwell 2D is an interactive software package for analyzing electric and magnetic fields with uniform cross-section or full rotational symmetry. In this paper, the eddy current field solver is used to simulate the eddy current effects of a radio frequency magnetic field in an electrical wire. The eddy current field solver calculates the eddy currents by solving A and φ in the field equation[5]:

$$\nabla \times \frac{1}{\mu}(\nabla \times A) = (\sigma + j\omega\varepsilon)(-j\omega A - V\varphi) \tag{3-4}$$

where A is the magnetic vector potential, φ is the electric scalar potential, μ is the relative magnetic permeability, σ is the conductivity, ε is the relative permittivity. The eddy current equation is derived from Maxwell equations:

$$\nabla \times \vec{H} = \vec{J} + \frac{\partial \vec{D}}{\partial t} \tag{3-5}$$

$$\nabla \times \vec{E} = -\frac{\partial \vec{B}}{\partial t} \tag{3-6}$$

$$\nabla \cdot \vec{D} = \rho \tag{3-7}$$

$$\nabla \cdot \vec{B} = 0 \tag{3-8}$$

where E is the electric field, D is the electric displacement, B is the magnetic flux density, H is the magnetic field intensity measured in units of A/m, J is the current density, and ρ is the charge density. These fundamental laws govern the existence of electrical and magnetic fields.

Using Euler's formula:

$$e^{j\alpha} = \cos\alpha + j\sin\alpha \tag{3-9}$$

If $\alpha = \omega t + \theta$, $F(t)$ equals the real portion of $e^{j(\omega t+\theta)}$:

$$F(t) = R[F_m e^{j(\omega t+\theta)}] = R\{F_m[\cos(\omega t+\theta) + j\sin(\omega t+\theta)]\} = F_m\cos(\omega t+\theta) \tag{3-10}$$

Because each time-varying quantity has the form $F_m e^{j\theta} e^{j\omega t}$, $\frac{\partial \vec{D}}{\partial t} = j\omega D$ and $\frac{\partial \vec{B}}{\partial t} = j\omega B$, with this simplification and the relations between vector D and E, B and H, J and E, J and V,

$$B = \mu H \tag{3-11}$$

$$D = \varepsilon E \tag{3-12}$$

$$J = \sigma E \tag{3-13}$$

$$J = \rho_V V \tag{3-14}$$

Maxwell equations reduce to

$$\nabla \times \frac{B}{\mu} = (\sigma E + j\omega\varepsilon E) \tag{3-15}$$

$$\nabla \times E = j\omega B \tag{3-16}$$

$$\nabla \cdot \varepsilon E = \rho \tag{3-17}$$

$$\nabla \cdot B = 0 \tag{3-18}$$

The quantity A, the magnetic vector potential, is solved by the eddy current field simulator. A is given by:

$$\nabla \times A = B \tag{3-19}$$

Substituting this formula into the first of Maxwell equations, the result is:

$$\nabla \times \frac{1}{\mu}(\nabla \times A) = (\sigma E + j\omega\varepsilon E) \tag{3-20}$$

$$E = -j\omega A - V\varphi \tag{3-21}$$

where φ is the electric potential. Substituting the right side of this relationship for E into the previous equation results in:

$$\nabla \times \frac{1}{\mu}(\nabla \times A) = (\sigma + j\omega\varepsilon)(-j\omega A - V\varphi) \tag{3-22}$$

This equation is one of the two used by the eddy current solver to compute A and φ.

3.2.2 Geometry definition of electrical wire model

In this chapter, we use the eddy current solver, XY plane in Maxwell 2D, to simulate the RF magnetic fields in an electrical wire. We assume the electrical wire in the implanted medical device is a cylindrical wire. The structure of the 3D field pattern can be modeled by simulating the fields in its cross-section. (See Figure 22.) Such a 2D structure can be analyzed more quickly and easily than a 3D structure.

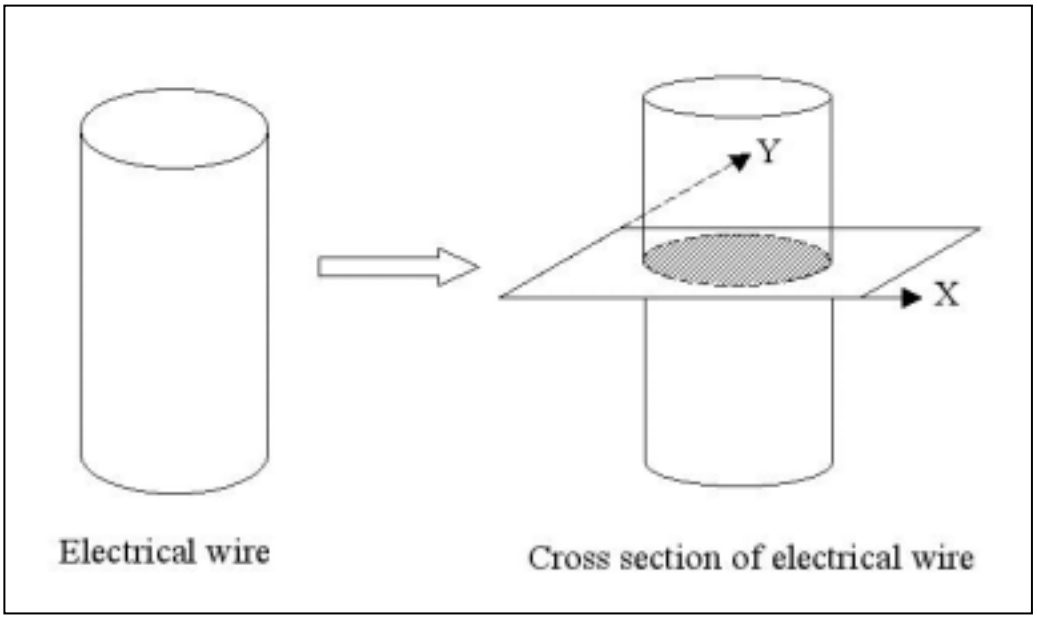

Figure 22. Transfer of the 3D model of electrical wire to 2D model

3.2.2.1 Radius definition

Due to the restriction of the software, the radius for the cross-section of the electrical wire mode must be carefully chosen. The radius of the electrical wire model should be larger than the skin depth in the wire induced by the RF magnetic field. Usually, the electrical wire of the implanted medical device is made of aluminum, which has the following parameters:

$$\mu_r = 1 \tag{3-23}$$

$$\sigma = 3.8 \times 10^7 \tag{3-24}$$

The skin depth for aluminum wire in 64 MHz MRI magnetic fields is,

$$\delta = \sqrt{\frac{1}{\pi f \mu_r \mu_0 \sigma}} = \sqrt{\frac{1}{\pi 64 \times 10^6 \times 4\pi \times 10^{-7} \times 3.8 \times 10^7}} = 10um \tag{3-25}$$

We choose 100um as the radius of cross-section for the electrical wire.

3.2.2.2 No shielding model and shielding model.

Figure 23 shows the cross-section of the electrical wire created in Maxwell 2D. The black circle in Figure 23 represents the cross-section of the electrical wire, with the radius set at $100\,\mu$m. The $1000 \times 1000\ \mu$m square represents the human body around the wire.

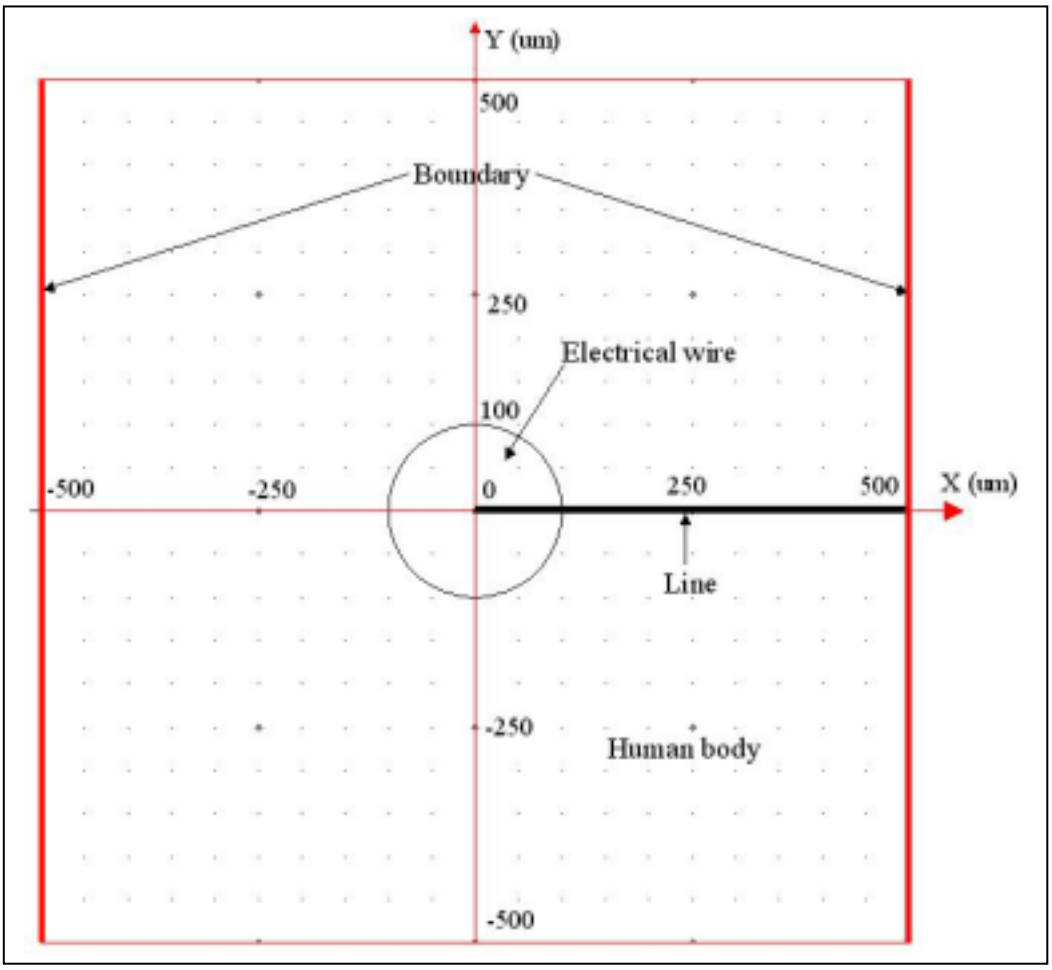

Figure 23. Electrical wire model in Maxwell 2D

Figure 24 shows a part of the enlarged shielding wire. The magnetic film is designed to coat on the surface of the wire for magnetic shielding. An insulating layer (1 μm in thickness) is inserted between the wire and the shielding layer for electricity insulating. Then the coated wire is inserted into the human body, which is represented by a square with dimensions set at 1000×1000 μm.

Altogether, there are four objects in the model: the wire, the insulating layer, the shielding layer, and the human body. The radius of the wire and the size of the human body region remain as constants. The thickness of the shielding layer varies from 100 nm to 10 μm. We will investigate how the shielding effect is affected by the shielding thickness.

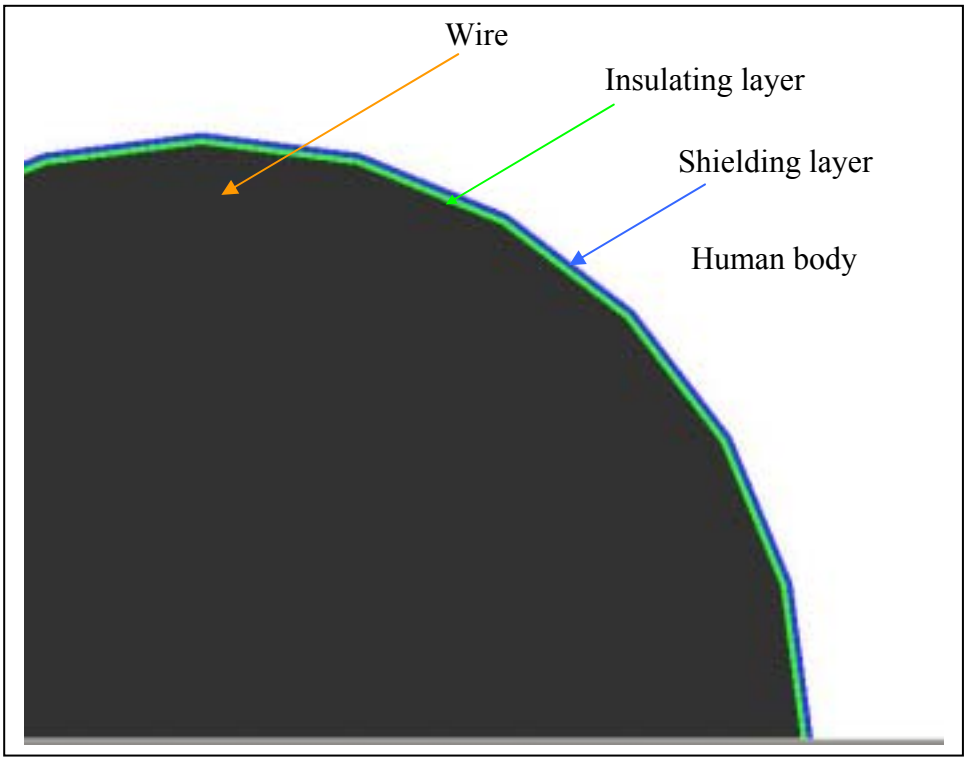

Figure 24. A quarter of an enlarged 2D shielding model in human body

3.2.3 Material assignment

Each of the objects in the model has been assigned a material. The properties associated with the material such as relative permeability, relative permittivity, and conductivity are assigned to the object. Usually, the electrical wire in the implanted medical device is made of aluminum, so aluminum is assigned as the material of the electrical wire, AlN is used as the insulating layer. The parameters of these assigned materials are listed in Table X.

Table X. Parameters of the Assigned Materials

Object	**Material**	**Parameters**		
		ε	μ	σ (siemens/meter)
Wire	Aluminum	1	1.0021	3.8×10^7
Insulating layer	AlN	8.8	1	0
Shielding layer	AlFe	1	*	*
Human body	Human body	80	1	1.8

where ε is permittivity (dielectric constant), the ratio of electric displacement in a dielectric medium to the applied electric field strength. This ratio indicates the degree to which the medium can resist the flow of electric charge. It is measured in farads per meter. μ is permeability, the ratio of the magnetic flux density in a body or medium to the external magnetic filed strength inducing it. It has the unit Henry per meter. σ is conductivity, a measure of the ability of a material to conduct an electric charge, the reciprocal of resistivity. Conductivity is measured in siemens per meter.

The parameters of aluminum and AlN come from the global database in Maxwell 2D[4]. The human body's properties are obtained from other literature[9].

In the computer simulation, these material parameters are set as constants. Only the permeability and conductivity of the shielding material is changed in order to see how the shielding effects are affected.

3.2.4 Boundary setup

The wire experiences the radio frequency magnetic field in MRI, which has the magnetic field strength at $10 \sim 20 \times 10^{-6}$ tesla and 64MHz in frequency.

To model such a magnetic field, the value boundary in Maxwell 2D eddy current solver is used to set the magnetic vector potential $A_z(t)$ to a constant value on a boundary. In the eddy current problems, the magnetic vector potential is a time-varying quantity in the form:

$$A_z(t) = A_m \cos(\omega t + \theta) \tag{3-27}$$

where A_m is the magnitude of the potential and θ is its phase angle. It offsets from a pure cosine wave.

3.2.4.1 Magnetic vector potential

The magnetic vector potential is defined by the following equation:

$$\nabla \times A = B \tag{3-28}$$

Since the eddy current fields solver assumes that A has a Z-component only and B lies in the XY-plane, the relationship of B and Z is expressed as:

$$\mathbf{B} = \frac{\partial A_z}{\partial Y} X - \frac{\partial A_z}{\partial X} Y \tag{3-29}$$

We set the right and left edges of the human body as the value boundary; therefore, the magnetic field is tangential to the boundaries. The direction of the magnetic field is in XY plane and along Y-axis. The magnitude of A_Z can be calculated as:

$$\mathbf{B}_Y = \frac{dA_z}{dX} \tag{3-30}$$

Assuming that B has only component $\mathbf{B}_X$, then in the Cartesian coordinate system:

$$\mathbf{B}_Y dX = d(A_Z) \tag{3-31}$$

Re-arranging the integration of both sides:

$$\int_0^{X_{\max}} \mathbf{B}_Y dX = \int d(A_z) \tag{3-32}$$

$$X_{\max} B_Y = A_Z \tag{3-33}$$

where A_Z is the magnetic vector potential which exists only in the Z direction, and $X_{\max}$ is the vertical distance from center of the electrical wire to the edge of the human body. In our project, a constant magnetic field of 20×10^{-6} tesla is applied. The vertical distance from center of the electrical wire to the edge of the human body is set at 500 μm, and the value for Az is:

$$A_Z = 20 \times 10^{-6}\,\text{Tesla} \times 500\mu m = 1 \times 10^{-8}\,\text{Webers}/\text{meter} \tag{3-34}$$

4 Results and Discussion

4.1 No shielding model

Figure 25 shows the magnetic distribution in the no shielding model.

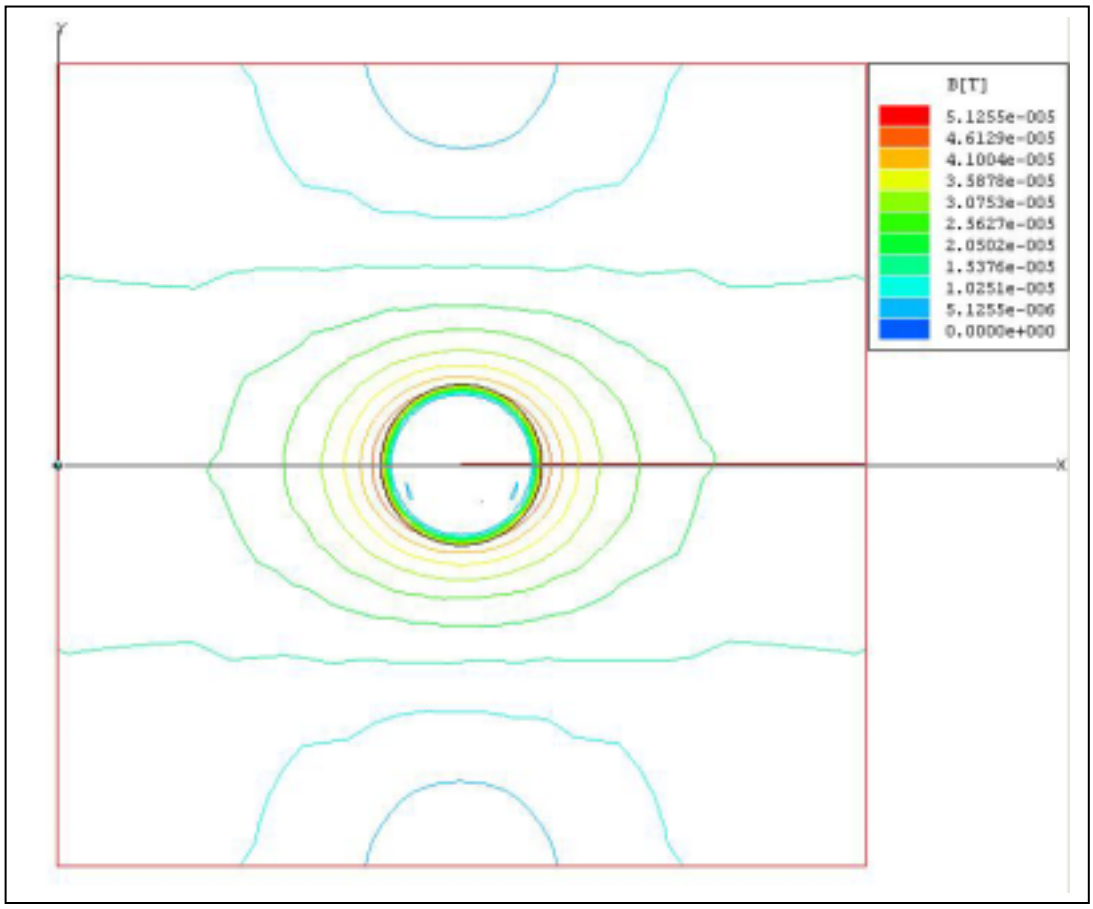

Figure 25. Magnetic distribution in the no shielding model

The aluminum wire is represented by a circle in the center, and various magnitudes of the flux density in tesla are represented by different colors. From the figure, we can see that the magnetic lines of force are concentrated toward the electrical wire.

To show clearly how the magnetic flux density is changed in the area inside the wire and outside the wire, a line is defined.

A line from the center of electrical wire to the right edge of the human body (X = 0 um to X =500 um) is drawn (see Figure 23). The magnitude of the magnetic flux density is plotted along the line as Figure 26 shows.

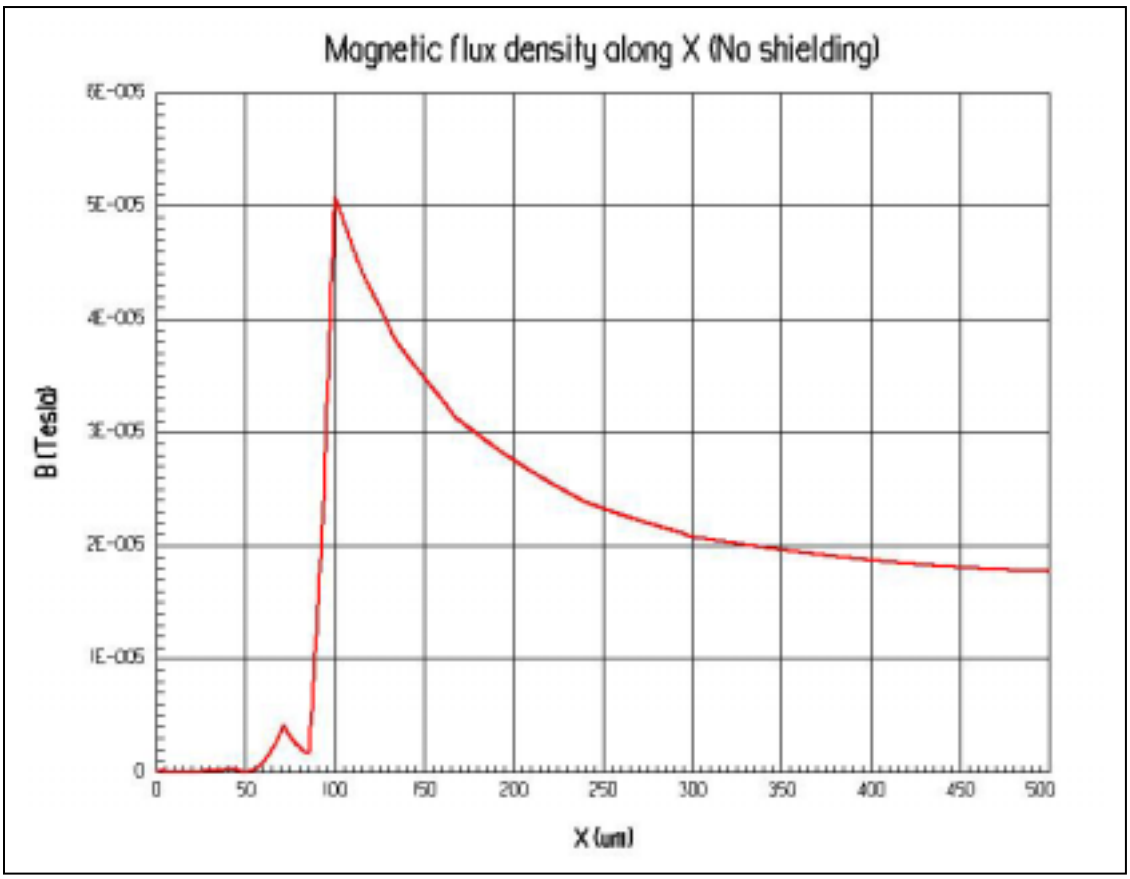

Figure 26. Magnetic flux density along X in no shielding model

From X=0 to X= 100 um is the electrical wire; above 100um is the human body. As shown in Figure 26, the magnetic flux density can only penetrate into a portion of the electrical wire (between X= 55 to X= 100). In the central area (from X = 0 to X = 55um), the magnetic flux density is almost 0. This is because the electrical wire is assigned as aluminum; as a conductor, it tends to deflect the magnetic lines of force, so that the flux density inside the wire becomes smaller. In the human body area surrounding the wire (from X = 100 to X = 500), the magnetic flux density decreases slowly, and then reaches 1.75×10^{-5} tesla at the boundary.

4.2 Shielding model

Some shielding models have been simulated to see how the shielding effects are affected by the shielding layer conductivity, permeability, and thickness. While one parameter varies, the other parameters are kept as constants.

4.2.1 Shielding conductivity model

In the shielding conductivity model, an electrical wire is shielded by a shielding material having conductivity σ and permeability μ ($\mu = 1$ is assumed). Shielding thickness is set at 1 μm , and the shielding conductivity σ varies from 1 to 1×10^8 siemens/meter . The average power loss can be calculated automatically in watts per meter. Figure 27 shows the relationship between the power loss and the conductivity of the shielding material. The permeability is plotted on a logarithmic scale.

The power loss remains as constant when the shielding conductivity increases from 1 to 10^5 siemens/meter ; then it increases accordingly as the shielding conductivity increases from 10^5 siemens/meter to 4×10^7 siemens/meter . After 4×10^7 siemens/meter , the power loss decreases quickly as the conductivity increases to 10^8 siemens/meter . This data are tabulated in Appendix B.

Figure 28 shows the magnetic flux density along the X-axis in a conductivity model; the conductivity of the shielding is set at 10^3 siemens/meter , and the shielding thickness is set at $1\,\mu\text{m}$, $\mu = 1$.

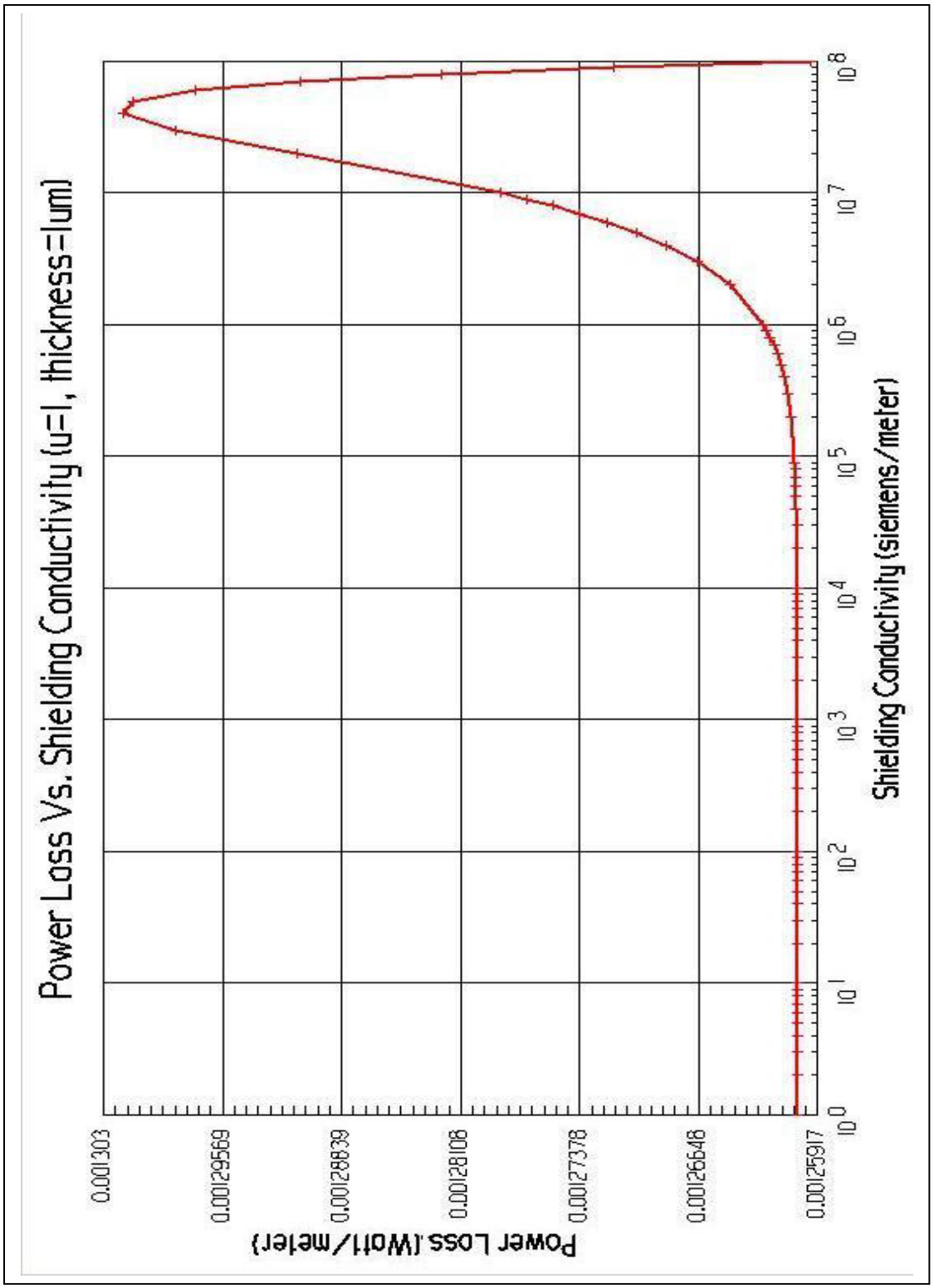

Figure 27. Power loss vs. shielding conductivity ($\mu = 1$, thickness = $1\,\mu m$)

Comparing the magnetic flux density along X in the no shielding model (Figure 26) with that of the conductive shielding model (Figure 28), we can see that the magnetic flux density in the human body region does not change. Only the first peak in the wire region changes from a sharp peak to a flat peak. The magnitude of this peak decreases after using a conductive shielding material.

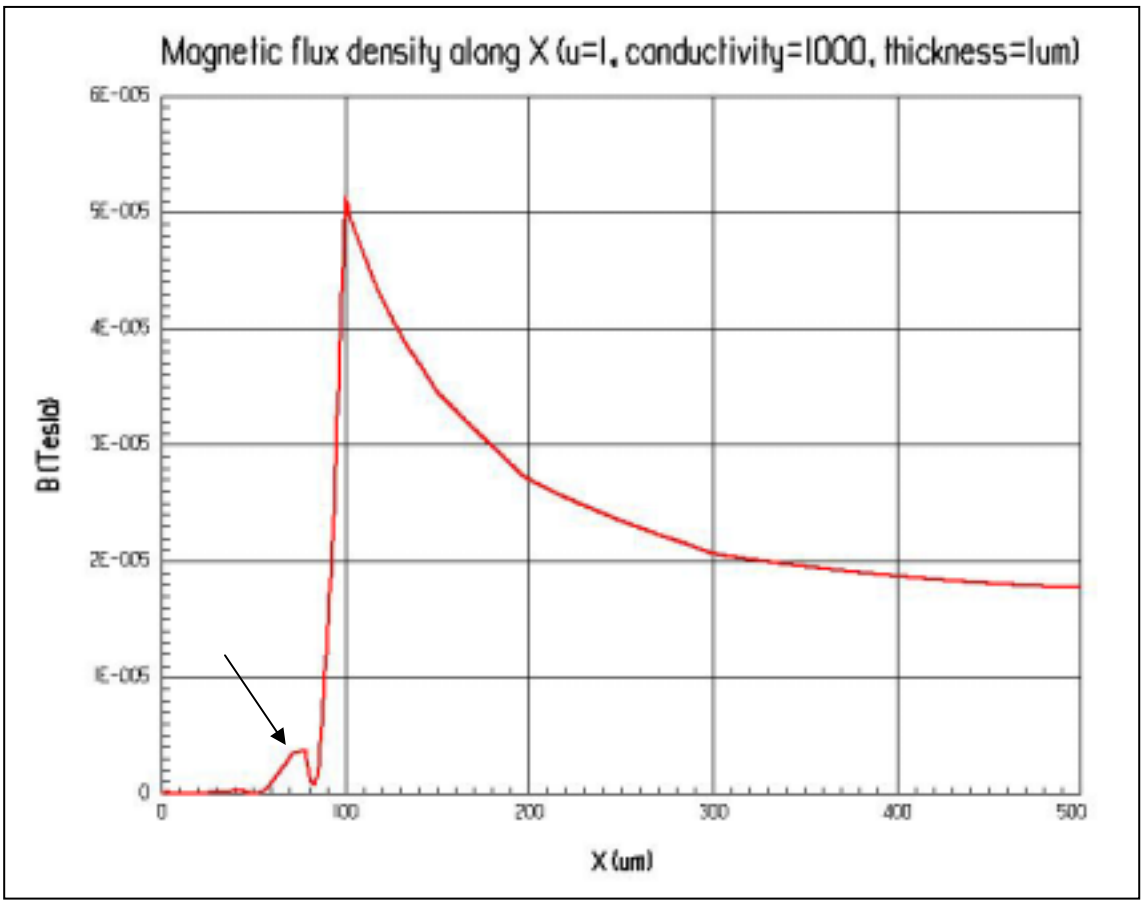

Figure 28. Magnetic flux density along X in a conductive shielding model (σ = 1000 siemens/meter , thickness = 1μm)

From the conductive shielding model, we can conclude that the conductive shell can shield the RF magnetic field. This shell tends to deflect the magnetic lines so that the magnetic flux density inside the shell becomes smaller[12]. Since the wire itself is a conductor, the skin effect acts as a conductive shielding; therefore, the magnetic flux density in the center of the conductive wire is 0 even in the no shielding mode. The 1-μm conductive shielding makes only a little difference in the shielding effect for a

conductive wire. Also, we can conclude that when other parameters of shielding material are given, the conductivity material should be set between the range of 1 to 10^5 siemens/meter in order to achieve a better shielding effect.

4.2.2 Shielding permeability model

In the shielding permeability model, an electrical wire is shielded by a material with conductivity σ and permeability μ, ($\sigma = 0$ is assumed). The shielding thickness is set at $1\,\mu m$, and the shielding permeability μ changes from 1 to 10^4. Figure 29 shows the relationship between the power loss and the permeability of the shielding material.

We can see that when the permeability increases, the power loss decreases. When $\mu < 10$, the slope is small. During the range of $1000 > \mu > 10$, the slope is very steep which means the power loss decreases quickly as the shielding permeability increases. When $\mu > 1000$, the slope becomes small again. The power loss does not change after $\mu > 3000$. This simulation data is tabulated in Appendix C.

From the shielding permeability model, we can see that for a given shielding thickness, increasing the shielding permeability results in a lower power loss, but after reaching the saturation point, this effect cannot be achieved any further. To get a better shielding effect, the permeability of the shielding material should be arranged at about 1000.

To investigate the magnetic flux density behavior along the X axis in a high permeable shielding material, a model with the following shielding parameters is simulated: shielding thickness = $1\,\mu m$, conductivity $\sigma = 0$, and permeability $\mu = 1000$. Figure 30 shows the variation of the magnetic flux density along the X-axis in this high permeable shielding model.

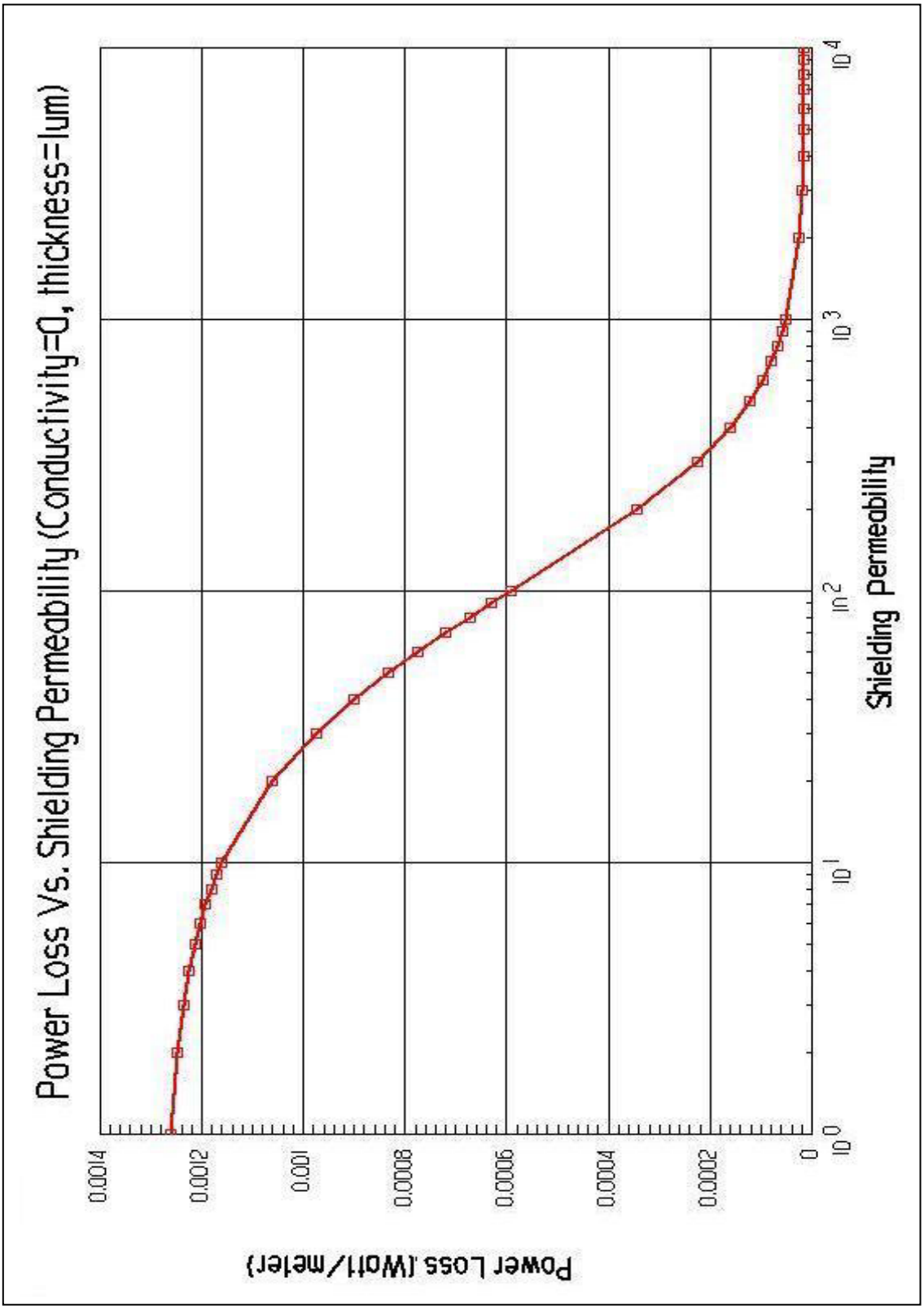

Figure 29. Power loss vs. shielding permeability (thickness = 1 μm , $\sigma = 0$)

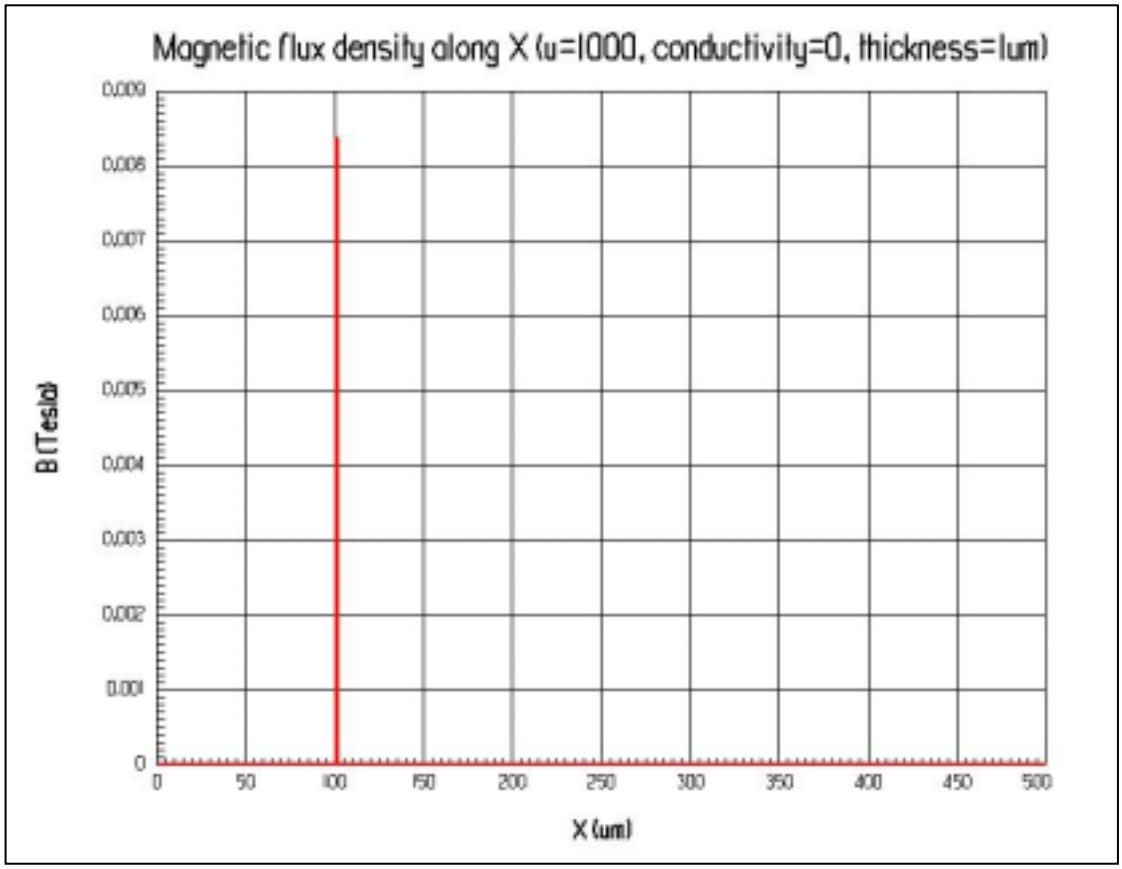

Figure 30. Magnetic flux density along X in a shielding permeability model ($\sigma = 0$, thickness = 1μm, $\mu = 1000$)

From Figure 30, we can see that, in the human body region, the magnetic flux density decreases to 0 tesla. The magnetic flux density in the shielding, however, is very high (about 0.0083 tesla) because of the high shielding permeability value of $\mu = 1000$. Since it is a ferromagnetic material, it tends to attract magnetic lines of force in the human body region surrounding it. The magnetic lines of force run mostly through the shell and leak very little outside it; therefore, the magnetic flux density in the human body region becomes smaller. Also the magnetic flux density in the wire region can be nearly neglected because the magnetic field strength outside the wire has decreased. Then the total magnetic flux, which transfers through the surface of the wire, decreases also. In addition to the skin effect, the total magnetic flux density in the wire becomes very small and can be neglected.

4.2.3 Shielding thickness model

The conductive shielding model and the permeable shielding model reveal the relationship between the shielding effect and the permeability/conductivity of the shielding material. To investigate the relationship between the shielding effect and shielding thickness, a shielding thickness model is established.

The above computer simulation results show that good values of permeability and conductivity of the shielding material are $\mu = 1000$, σ ¡Ü10^5 siemens/meter. In the shielding thickness model, we set the parameters as $\mu = 1000$ and $\sigma = 1000$ siemens/meter; the shielding thickness varies from 100nm to 10um.

Figure 31 shows how the power loss is affected by the shielding thickness. Figure 31 also shows that when the shielding thickness is less than 2 um, the power loss decreases quickly while the shielding thickness increases. When the thickness is greater than 2um, the power loss does not change with the increase in shielding thickness. The data are tabulated in Appendix D.

We can conclude that increasing the thickness up to a threshold value results in a lower power loss. A lower power loss means a better shielding effect. But it is not meaningful to use a thick shielding if the same shielding effect can be achieved with a relatively thin shielding layer. In the model described above, the desired minimum shielding thickness is 2um.

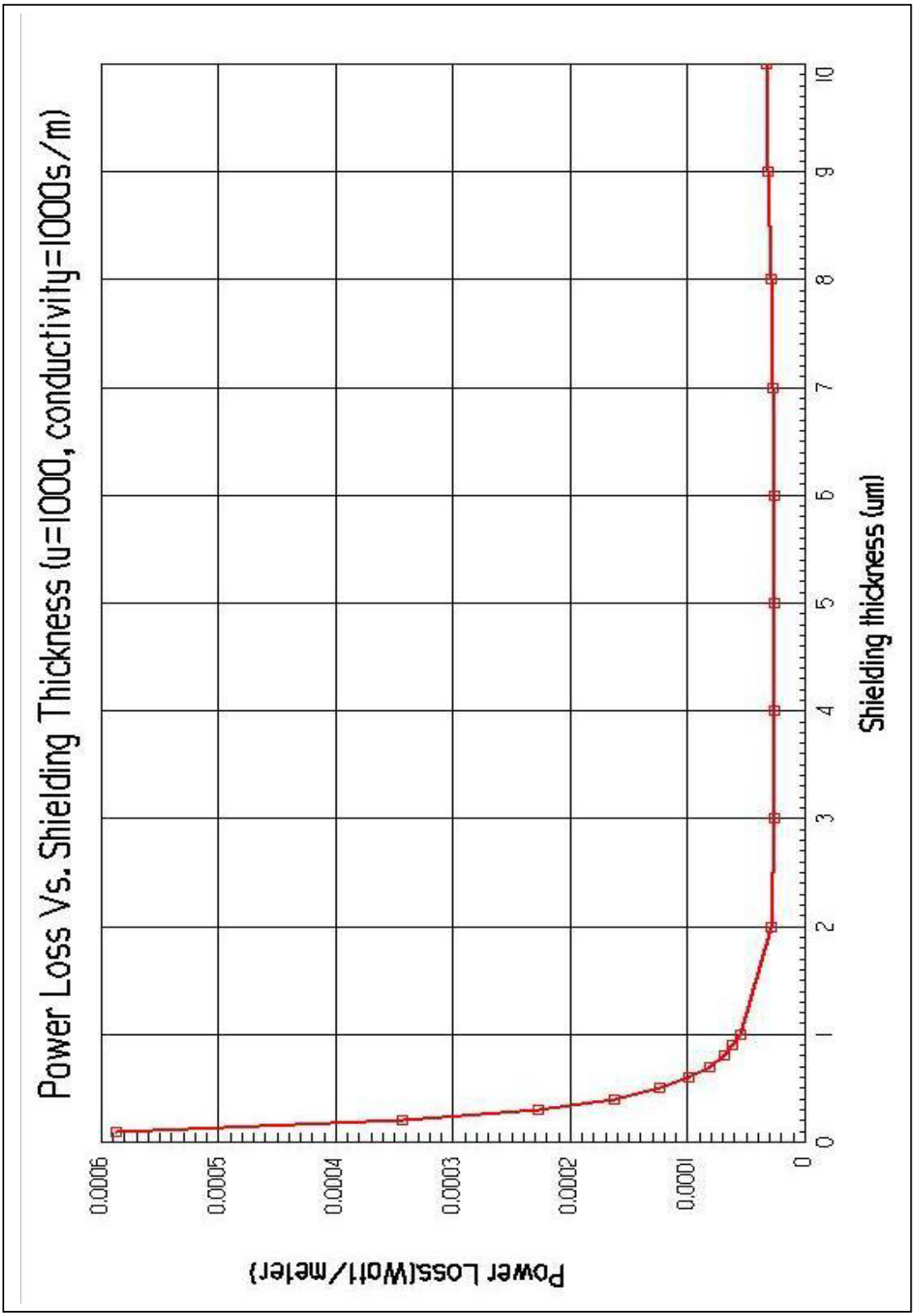

Figure 31. Power loss vs. shielding thickness ($\mu = 1000$, $\sigma = 1000$)

4.2.4 As-deposited AlFe film shielding model

In the as-deposited AlFe film shielding model, the as-deposited AlFe film is assigned to be the shielding material. Since the thickness of the as-deposited AlFe films range from 130nm to 1um, the conductivity of the films is in the order of 10^4 siemems/meter , and the magnetic permeability ranges from 20 to 100. We performed a computer simulation to see the shielding effect when the as-deposited AlFe films are assigned as shielding materials.

Figure 32 illustrates the power loss versus the shielding permeability at various shielding thickness. The permeability changes from 20 to 100. The shielding conductivity is set at 10000 siemens/meter . Various shielding thickness of 150nm, 500nm, 1um, and 2um are selected for simulation to compare their power loss.

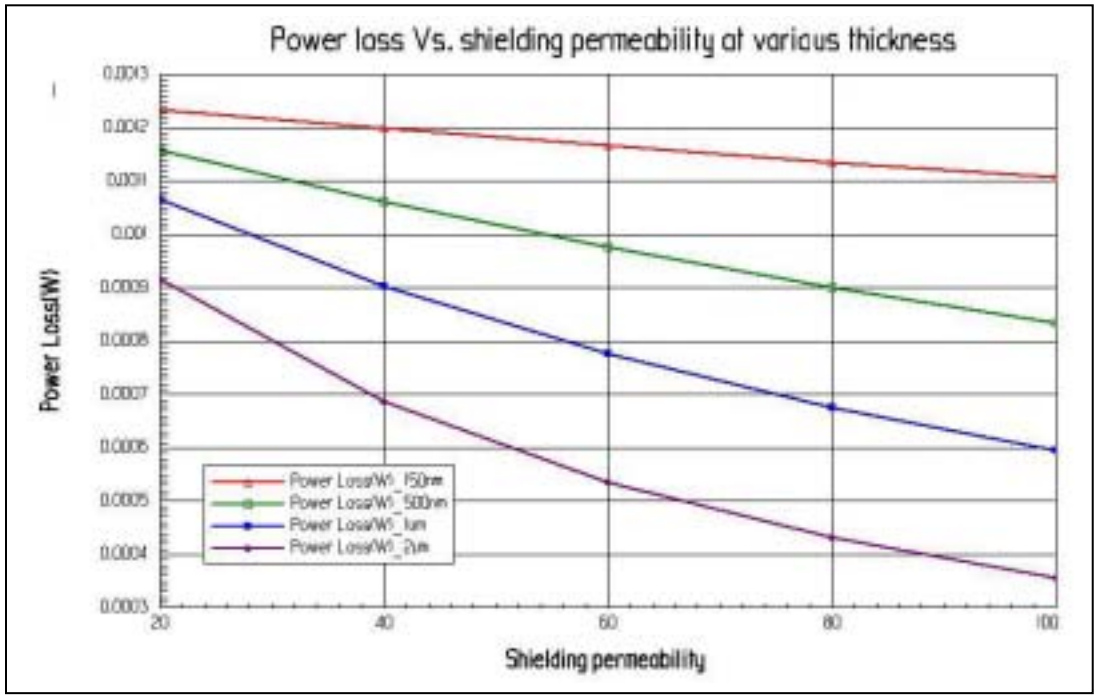

Figure 32. Power loss vs. shielding permeability at various thicknesses

Figure 32 show that the power loss decreases as the permeability increases from 20 to 100 for all the four shielding thickness: 150nm, 500nm, 1um, and 2um. But the gradient is different. The 150nm as-deposited AlFe film has the lowest gradient, and the 2um as-deposited film has the highest gradient.

The power loss data is shown in Table XI.

Table XI. Power Loss Vs. Shielding Permeability at Various Thickness (σ = 10000 siemens/meter)

σ (siemens/meter)	Thickness (um)	μ	Power Loss (watt/meter)
10000	0.15	20	1.23346e-003
		40	1.19968e-003
		60	1.16730e-003
		80	1.13623e-003
		100	1.10642e-003
	0.5	20	1.15883e-003
		40	1.06123e-003
		60	9.75702e-004
		80	9.00303e-004
		100	8.33479e-004
	1	20	1.06555e-003
		40	9.04179e-004
		60	7.77583e-004
		80	6.76410e-004
		100	5.94278e-004
	2	20	9.15915e-004
		40	6.86275e-004
		60	5.35723e-004
		80	4.31804e-004
		100	3.57153e-004

We can see that in the as-deposited shielding films, the 2um as-deposited AlFe film with a permeability of 100 has the lowest power loss (3.57×10^{-4} watt/meter). In other words, this film has the best shielding effect among all the as-deposited AlFe films. The magnetic flux distribution in the 2um as-deposited AlFe film ($\mu=100$) shielding model is illustrated in Figure 33.

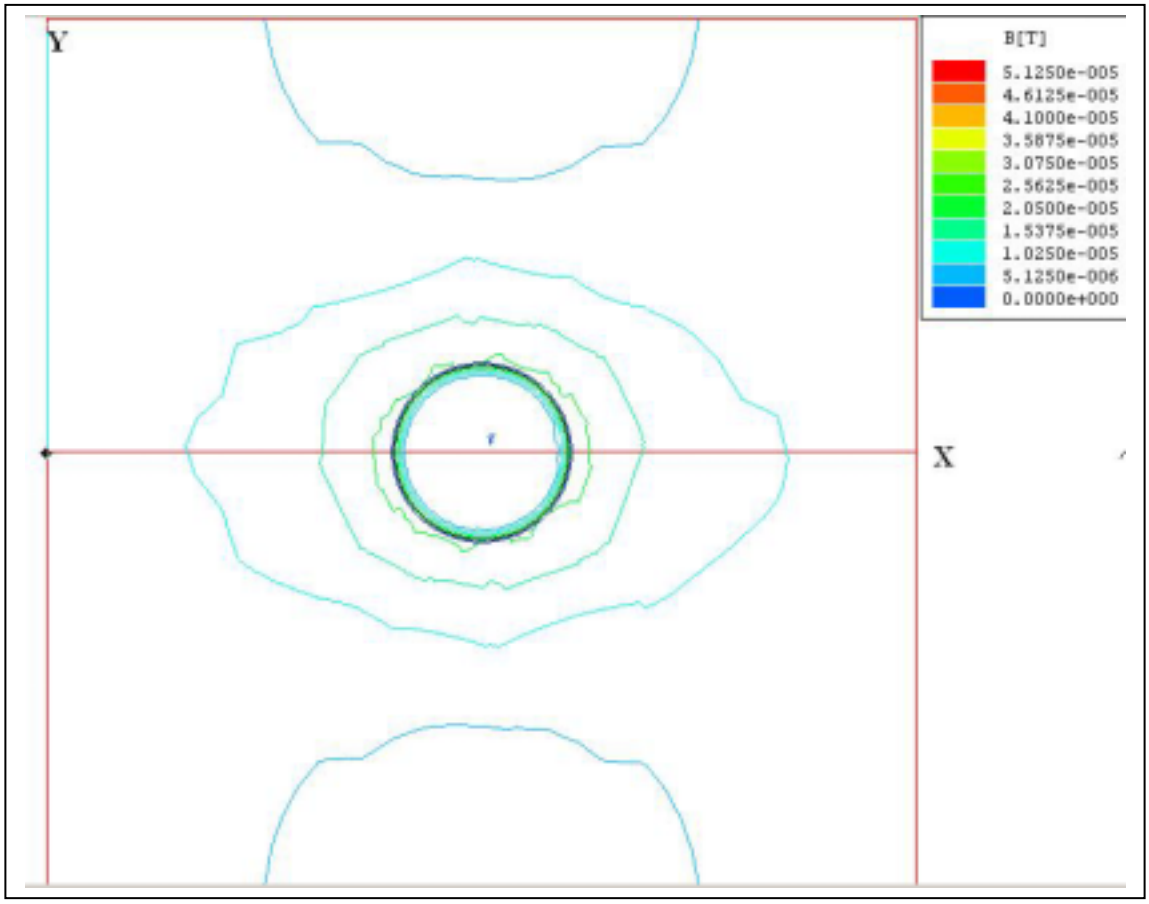

Figure 33. Magnetic distribution in the 2um as-deposited AlFe shielding model ($\mu=100, \sigma=10000$)

Comparing the magnetic distribution in the 2um as-deposited AlFe shielding model (Figure 33) with that of the no shielding model (Figure 25), we can see that there are still some magnetic lines existing in the wire and in the human body region. However, the magnetic flux density in both areas has decreased.

Also a line is drawn from the center of the wire to the right edge of the human body region. The variation of the magnetic flux density along this line is shown in Figure 34.

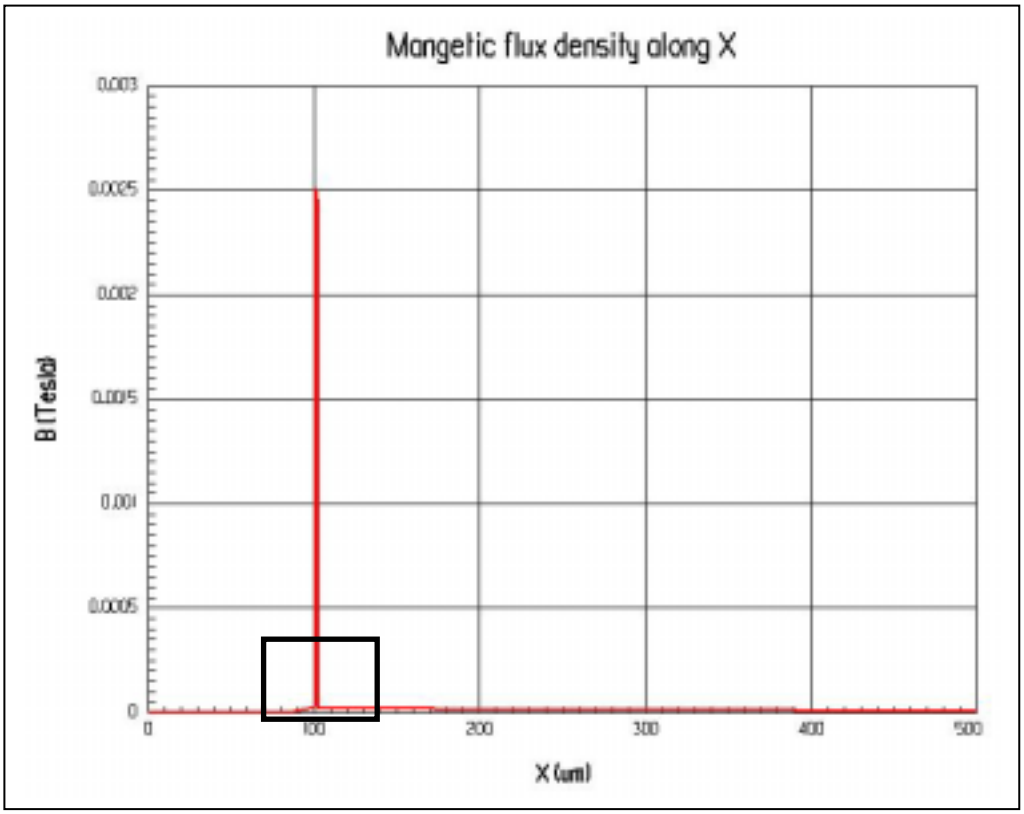

Figure 34. Magnetic flux density along the X-axis in the as-deposited AlFe film shielding model ($\mu = 100$, $\sigma = 10000$ siemens/meter , thickness = 2μm)

In Figure 34, the region from $X = 0$ μm to $X = 100$ μm is the electrical wire; the region from $X = 100$ μm to $X = 101$ μm is the as-deposited AlN film insulating layer; and the region from $X = 101$ μm to $X = 103$ μm is the AlFe shielding layer (the thickness of the AlFe film is 2 μm). In the AlFe shielding layer, the magnetic flux density is 0.0025 tesla. Figure 35 gives more detailed information from the enlarged rectangle region in Figure 34. As we can see, the magnetic flux density from $X = 0$ μm to $X = 87$ μm is about 0 tesla; then it increases slowly and reaches 2.5×10^{-5} tesla at the outermost surface of the electric wire. In the human body region, the magnetic flux density decreases suddenly to 2.1×10^{-5} tesla, and then does not change.

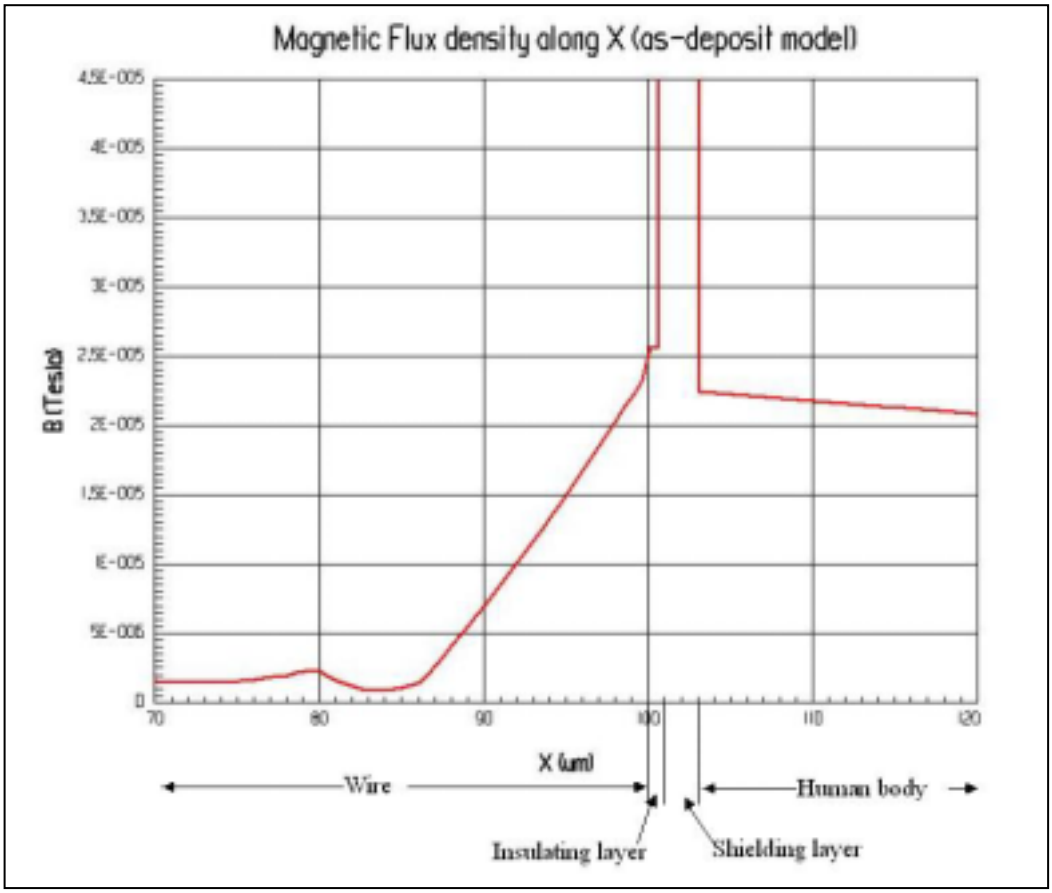

Figure 35. Enlargement figure for the rectangular area in Figure 34

The as-deposited AlFe film displays some ferromagnetic behavior. This film also has certain electrical conductivity. As a magnetic material, the magnetic lines of force in the space are concentrated near it. Notice that the magnetic permeability is 100. The magnetic flux density in the AlFe film is much higher than the originally-applied value. In Figure 35, the maximum value is 0.0025 tesla. (In the case of the 1,000 permeability value, the maximum value is 0.0083 tesla . See Figure 30.) The magnetic flux density in the human body region near the film surface is lower than that in the no-shielding model. (See Figure 26.) As a conductive material, the film behaves similarly to the film displayed in Figure 28. The combined effects due to both magnetic and electrical-conductive properties decrease the flux density in the wire.

4.3 Calculation of the heating from power loss

The temperature change of the aluminum wire when exposed to the RF magnetic field in the MRI procedure can be calculated according to its power loss. The temperature change ΔT can be calculated as:

$$\Delta T = \frac{\text{power loss} \times t}{M \times \text{specific heat}} \tag{4-1}$$

where t is the time for an MRI process, and M is the mass of the aluminum wire.

Usually, the process of MRI will last for at least 10 minutes, perhaps up to an hour; we assume the process is 10 minutes. The specific heat of aluminum is as follows: $q = 0.214 cal / g^{o}C$, and 1 calorie $= 4.18J$. The mass of the aluminum wire is calculated as $M = V \times D$, where D is the density of aluminum wire ($D = 2.7 g/cm^3$) and V is the volume of the aluminum wire.

In the Maxwell 2D simulation, the model is a cross-section of the aluminum wire, with the radius set at 100um. We assume the length of the wire is L cm. Then the volume of the aluminum wire can be expressed as:

$$V = \pi \times r^2 L = \pi (100 \mu m)^2 L = \pi \times L 10^{-4} cm^3 \tag{4-2}$$

$$\Delta T = \frac{\text{power loss} \times (L \times 10^{-2}) m \times 10 \min \times 60 \sec / \min}{2.7 g/cm^3 \times \pi \times L 10^{-4} cm^3 \times 0.214 \, cal/g^{o}C \times 4.18J} = 7915.57 \times \text{power loss} \tag{4-3}$$

According to the Maxwell 2D simulation results, the power loss for the no shielding model is 1.278×10^{-3} watt/meter. Then the temperature increase in the aluminum wire when the wire is exposed to the 64MHz RF magnetic field in MRI will be:

$$\Delta T = 7915.57 \times 1.278 \times 10^{-3} = 10.1^{o}C \tag{4-4}$$

The power loss for the 2um as-deposited AlFe shielding model is 3.57×10^{-4} watt/meter. Then the temperature increase in the aluminum wire when the shielding wire is exposed to the 64MHz RF magnetic field in MRI for 10 minutes will be,

$$\Delta T = 7915.57 \times 3.57 \times 10^{-4} = 2.8^{o}C \tag{4-5}$$

From the above calculation, we can see that when the no shielding aluminum wire is exposed to the RF magnetic field in the MRI procedure, the heating causes the

temperature to increase about $10.1^{o}C$. After shielding with the 2um as-deposited AlFe film, the heating in the wire causes the temperature to increase only by $2.8^{o}C$. The USFDA recommends that exposure to RF energy be limited. Any pulse sequence must not raise the temperature by more than 1^{o} Celsius.[3] In our calculations, the heat dissipation of the AlN and the human body are not taken into consideration. Since AlN is a very good heat conductive material, the overall temperature increase in the wire with shielding should remain within the acceptable level.

4.4 Optimal shielding model

From the formula (4-5), we can see the relationship between the power loss and the raised temperature. To keep the raised temperature below 1^{o} Celsius, the power loss should fulfill the following condition:

$$\Delta T < 1^{o}C \Rightarrow \text{power loss} < 1.26 \times 10^{4} \text{ Watt/meter} \quad (4\text{-}6)$$

From the above permeable shielding model, we can see that the power loss decreases when the magnetic permeability increases from 100nm to 1um.

The power loss of the as-deposited AlFe shielding model is very close to the desired value. For the optimal shielding model, we increase the permeability of the shielding material from just 100 to 300, while keeping the shielding conductivity and permeability as constants ($\sigma = 10000$ siemens/meter , thickness $= 2\mu$m). The power loss versus permeability of the optimal shielding model is plotted in Figure 36. We can see that when the permeability increases to 280, the power loss almost reaches 1.26×10^{4} Watt/meter. Power loss data around the permeability of 280 are listed in Table XII.

Table XII. Power Loss in Optimal Shielding Model

Shielding permeability	Power Loss (Watt/meter)
260	1.37418e-004
270	1.32204e-004
280	1.27405e-004
290	1.22980e-004

300	1.18890e-004

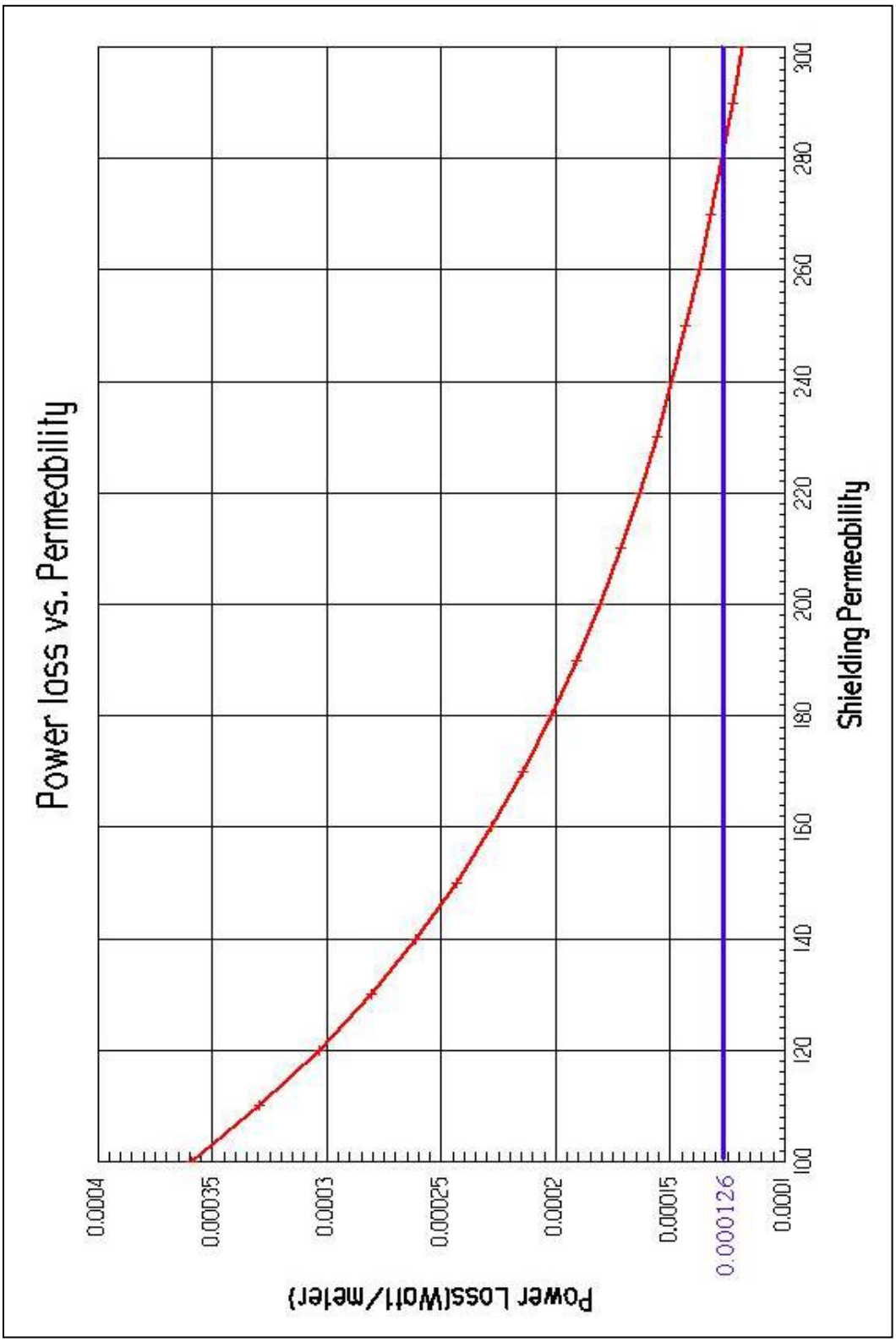

Figure 36. Optimal shielding permeability

5 Summary and Conclusions

5.1 Thin film deposition and characterization

Two kinds of thin films, aluminum iron (AlFe) and aluminum nitride (AlN), are deposited onto silicon wafers using sputtering deposition. The properties of both films have been analyzed using multiple methods.

For the as-deposited AlFe films, the thickness ranges from 130nm to 2um. Conductivity is in the order of 10^4 siemens/meter . Permeability is between 20 and 100.

5.2 Shielding computer simulation

A computer simulation model of the no shielding electrical wire was setup using Maxwell 2D. The computer simulation shows that the eddy current induced power loss occurs in the aluminum wire when it is exposed to the 64MHz RF magnetic field during the MRI procedure. The power loss is 0.001278 watt/meter in the no shielding electrical wire. Power loss related heating causes the wire temperature to increase by $10.1^{o}\mathrm{C}$.

Shielding computer simulations have been performed by changing the shielding thickness, conductivity, and permeability of the shielding material to see how the shielding effect (compared by power loss and magnetic flux density) is affected by these parameters. The results show the following:

The power loss increases accordingly as the shielding conductivity increases within a certain range (from 10^5 siemens/meter to 4×10^7 siemens/meter). After 4×10^7 siemens/meter , the power loss decreases quickly as the conductivity increases to 10^8 siemens/meter . The conductive shielding model shows that the magnetic flux density in the region inside the conductive shell is very small because the conductive shell tends to deflect the magnetic lines of force.

The power loss decreases as the permeability of shielding increases; above the saturation point, the power loss cannot be lowered just by increasing the shielding permeability. The magnetic flux density in the permeable shell increases a lot. This

density in the region around the magnetic shell becomes smaller because the shell tends to attract the magnetic lines of force.

The power loss decreases as the shielding thickness increases. After a certain point (the saturation point), increasing the shielding thickness does not decrease the power loss.

As-deposited AlFe film used as the shielding material is simulated in order to see if this film can shield the 64MHz RF magnetic field or not. The result shows that the power loss has decreased in the wire shielded with the as-deposited AlFe film compared to that without shielding. The power loss-related temperature increases by $2.8^{o}\mathrm{C}$.

To maintain the increased temperature within the acceptable level (1^{o} Celsius), power loss in the wire must be less than 1.26×10^{-4} Watt/meter. A possible approach is to increase the permeability of the as-deposited AlFe film above 280 and to keep the thickness at 2um and the conductivity in the order of 10^{4} siemens/meter.

6 Future Work

Optimal parameters for shielding the electrical wire from the 64MHz RF magnetic field have been obtained by computer simulation. Until now, no material with such properties has been reported.

The as-deposited AlFe film is a possible material to fulfill such requirements. This study shows that the as-deposited AlFe can shield part, but not all, of the 64MHz RF magnetic field. The possible reason is that the permeability of the film is not high enough.

Since the permeability of AlFe film is related to the percentage of Fe, maybe we can change the experiment conditions during sputtering deposition and get a higher percentage of Fe. The direct relationship between the permeability and the percentage of Fe in a thin AlFe film is not clear. Further study to clarify this relationship is needed.

On the other hand, increasing the percentage of Fe might increase the conductivity at the same time. As the shielding conductivity model shows, the conductivity of the film should not exceed 10^5 siemens/meter since the increased conductivity will result in an increase in power loss. When the material is deposited for magnetic shielding purposes, these two opposite effects must be offset.

When the temperature increase in the wire was calculated from the simulation result, the heat dissipation of the AlN insulating layer and the human body was not considered. These effects should be considered in future studies in order to achieve more accurate temperature calculations.

This study considers only the shielding properties of conductivity, permeability, and thickness. When the material with optimal properties becomes available, in vivo experiments should be performed. Such real-life experiments will significantly improve the computer simulation model.

7 References

1. *Harrison's Principles of Internal Medicine*, 12th ed.; p.867, 907. Edited by J. D.Wilson, E. Braunwald, K. J. Isselbacher, R. G. Petersdorf, J. B. Martin, A. S. Fauci, and R. K. Root. McGraw-Hill, New York, 1991.

2. J. Miles, "Spinal Cord Stimulators and spinal pumps for coccyx pain"(2002) Accessed on: March, 2003. Available at <http://www.coccyx.org/treatmen/spinstim.htm>

3. C. D. Smith, A. V. Kildishev, J. A. Nyenhuis, K. S. Foster, and J. D. Bourland, "Interactions of Magnetic Resonance Imaging Radio Frequency Magnetic Fields with Elongated Medical Implants,"*J. Appl. Phys.*, **87** [9] 6188-6190 (2000).

4. G. Zeman and S. D. Chap "Magnetic Resonance Imaging"(1956) Health Physics Society. Accessed on: July, 2002. Available at <http://hps.org/hpspublications/articles/mri.html>

5. Maxwell 2D, Material Property Database. Version 9.0. Ansoft Corporation, Pittsburgh, PA, 2002.

6. C. Suryanarayana and M. G. Norton, *X-Ray Diffraction: A Practical Approach*. New York, 1998.

7. C. A. Bayne, *Applied Electricity and Electronics*; p. 381, 403. Tinley Park, Illinois 1999.

8. R. Ludwig and P. Bretchko, *RF Circuit Design: Theory and Applications*; p.11. Prentic Hall, Upper Saddle River, New Jersey, 2000.

9. "The Human Body in the Presence of Electromagnetic Spectrum"(1980) MIT Media Lab. Accessed on: September, 2002. Available at < http://web.media.mit.edu/~giri/physproj/node8.html>

10. G. Bonmassar, L. Angelone, F. Segonne, A. Potthast, B. Fischl, L. Wald, and J. Belliveau, " SAR Computations in a Realistic and High-Resolution Model of the Head with EEG Electrodes in Place"Accessed on: January, 2003. Available at <http://www.academicpress.com/www/journal/hbm2002/15211.html>

11. J. J Cathey and S. A. Nasar, *Shaum's Outline of Theory and Problems of Basic Electrical Engineering*; 2nd ed. McGraw-Hill, New York, 1997.

12. T. Rikitake, *Magnetic and Electromagnetic Shielding*; p.15, p.164-165. Terra Scientific, Tokyo, Japan, 1987.

Appendix A. Conversion between S.I. system and cgs units

Parameter	SI system	*cgs* unit	Conversion
Magnetic moment (m)	Am^2	*emu*	$1Am^2 = 10^3 emu$
Magnetization (M)	Am^2	emu/cm^3	$1Am^{-1} = 10^3 emu/cm^3$
Magnetic field (H)	Am^2	Oersted (oe)	$1Am^{-1} = 4\pi \times 10^{-3} oe$
Magnetic Induction (B)	T	Gauss (G)	$1T = 10^4 G$
Permeability of free space (μ_0)	Hm^{-1}	1	$4\pi \times 10^{-7} Hm^{-1} = 1$

$*1H = kg * m^2 A^{-2} s^{-2}$, $1emu = 1Gcm^3$, $B = \mu_0 (H + M)$, $1T = kgA^{-1}s^{-2}$

Appendix B. Power loss vs. shielding conductivity

($\mu = 1$, thickness = 1 um)

Shielding conductivity (Siemens/meter)	Power Loss (Watt/meter)
1.00000e+000	1.26039e-003
2.00000e+000	1.26039e-003
3.00000e+000	1.26039e-003
4.00000e+000	1.26039e-003
5.00000e+000	1.26039e-003
6.00000e+000	1.26039e-003
7.00000e+000	1.26039e-003
8.00000e+000	1.26039e-003
9.00000e+000	1.26039e-003
1.00000e+001	1.26039e-003
2.00000e+001	1.26039e-003
3.00000e+001	1.26039e-003
4.00000e+001	1.26039e-003
5.00000e+001	1.26039e-003
6.00000e+001	1.26039e-003
7.00000e+001	1.26039e-003
8.00000e+001	1.26039e-003
9.00000e+001	1.26039e-003
1.00000e+002	1.26039e-003
2.00000e+002	1.26039e-003
3.00000e+002	1.26039e-003
4.00000e+002	1.26039e-003
5.00000e+002	1.26039e-003
6.00000e+002	1.26040e-003
7.00000e+002	1.26040e-003

8.00000e+002	1.26040e-003
9.00000e+002	1.26040e-003
1.00000e+003	1.26040e-003
2.00000e+003	1.26040e-003
3.00000e+003	1.26040e-003
4.00000e+003	1.26040e-003
5.00000e+003	1.26040e-003
6.00000e+003	1.26041e-003
7.00000e+003	1.26041e-003
8.00000e+003	1.26041e-003
9.00000e+003	1.26041e-003
1.00000e+004	1.26042e-003
2.00000e+004	1.26044e-003
3.00000e+004	1.26046e-003
4.00000e+004	1.26048e-003
5.00000e+004	1.26050e-003
6.00000e+004	1.26052e-003
7.00000e+004	1.26054e-003
8.00000e+004	1.26056e-003
9.00000e+004	1.26059e-003
1.00000e+005	1.26061e-003
2.00000e+005	1.26082e-003
3.00000e+005	1.26103e-003
4.00000e+005	1.26124e-003
5.00000e+005	1.26145e-003
6.00000e+005	1.26166e-003
7.00000e+005	1.26187e-003
8.00000e+005	1.26208e-003
9.00000e+005	1.26229e-003

1.00000e+006	1.26250e-003
2.00000e+006	1.26454e-003
3.00000e+006	1.26651e-003
4.00000e+006	1.26842e-003
5.00000e+006	1.27027e-003
6.00000e+006	1.27206e-003
7.00000e+006	1.27379e-003
8.00000e+006	1.27546e-003
9.00000e+006	1.27707e-003
1.00000e+007	1.27863e-003
2.00000e+007	1.29113e-003
3.00000e+007	1.29861e-003
4.00000e+007	1.30176e-003
5.00000e+007	1.30118e-003
6.00000e+007	1.29742e-003
7.00000e+007	1.29098e-003
8.00000e+007	1.28228e-003
9.00000e+007	1.27172e-003
1.00000e+008	1.25962e-003

Appendix C. Power loss vs. shielding permeability

(σ = 0 , thickness = 1 um)

Shielding Permeability	Power Loss (Watt/meter)
1.00000e+000	1.26039e-003
2.00000e+000	1.24849e-003
3.00000e+000	1.23683e-003
4.00000e+000	1.22534e-003
5.00000e+000	1.21403e-003
6.00000e+000	1.20288e-003
7.00000e+000	1.19189e-003
8.00000e+000	1.18105e-003
9.00000e+000	1.17037e-003
1.00000e+001	1.15983e-003
2.00000e+001	1.06203e-003
3.00000e+001	9.76319e-004
4.00000e+001	9.00741e-004
5.00000e+001	8.33743e-004
6.00000e+001	7.74063e-004
7.00000e+001	7.20669e-004
8.00000e+001	6.72704e-004
9.00000e+001	6.29455e-004
1.00000e+002	5.90323e-004
2.00000e+002	3.42976e-004
3.00000e+002	2.26192e-004
4.00000e+002	1.61998e-004
5.00000e+002	1.22997e-004
6.00000e+002	9.75566e-005
7.00000e+002	8.00562e-005

8.00000e+002	6.75101e-005
9.00000e+002	5.82140e-005
1.00000e+003	5.11376e-005
2.00000e+003	2.50089e-005
3.00000e+003	1.92403e-005
4.00000e+003	1.71077e-005
5.00000e+003	1.61010e-005
6.00000e+003	1.55517e-005
7.00000e+003	1.52218e-005
8.00000e+003	1.50097e-005
9.00000e+003	1.48661e-005
1.00000e+004	1.47649e-005

Appendix D. Power loss vs. shielding thickness

($\mu = 1000$, $\sigma = 1000$ siemens/meter)

Shielding thickness (μm)	Power Loss (Watt/meter)
1.00000e-001	5.87079e-004
2.00000e-001	3.42759e-004
3.00000e-001	2.27248e-004
4.00000e-001	1.63305e-004
5.00000e-001	1.24331e-004
6.00000e-001	9.87356e-005
7.00000e-001	8.14207e-005
8.00000e-001	6.89478e-005
9.00000e-001	6.23427e-005
1.00000e+000	5.51212e-005
2.00000e+000	2.87902e-005
3.00000e+000	2.59672e-005
4.00000e+000	2.57390e-005
5.00000e+000	2.58160e-005
6.00000e+000	2.67133e-005
7.00000e+000	2.80245e-005
8.00000e+000	2.95755e-005
9.00000e+000	3.12812e-005
1.00000e+001	3.30964e-005